THESIS FOR THE DEGREE OF DOCTOR OF PHILOSOPHY

In-Band Full-Duplex Antenna Systems

Mustafa Ayebe



Antenna Systems Group
Department of Electrical Engineering
Chalmers University of Technology
Gothenburg, Sweden, 2026

In-Band Full-Duplex Antenna Systems

Mustafa Ayebe

Copyright © 2026 Mustafa Ayebe except where otherwise stated.

ISBN 978-91-8103-502-5
Series number 5959
ISSN 0346-718X
DOI 10.63959/chalmers.dt/5959

Department of Electrical Engineering
Chalmers University of Technology
SE-412 96 Gothenburg, Sweden
Phone: +46 (0)31 772 1000
www.chalmers.se

Printed by Chalmers Digital Printing
Gothenburg, Sweden, November 2026

Her daim yanımda olan aileme ithafen.

Abstract

In-band full-duplex (IBFD) systems transmit and receive simultaneously in the same frequency band, promising higher spectral efficiency for communication and new capabilities in radar sensing. In practice, the transmitter's own signal couples into the receiver as self-interference (SI), which can be many orders of magnitude stronger than the desired signal and saturate the receiver front end. This thesis investigates antenna- and beamforming-based techniques for mitigating SI while preserving the desired radiation and reception performance of full-duplex antenna arrays.

An analytical framework is developed for non-shared-aperture IBFD antenna arrays using scattering parameters, power-wave representations, and embedded element patterns. Within this framework, transmit (Tx) beamforming is formulated as a constrained optimization problem that maximizes array gain while controlling SI coupled to the receive (Rx) array. The solution lies in a low-coupling Tx subspace obtained from an eigenvalue problem, whose dimension sets the available degrees of freedom. Rx beamforming is then employed to suppress residual SI while preserving the desired signal. The framework is subsequently extended to IBFD multi-user multiple-input multiple-output (MU-MIMO) systems, combining SI-constrained Tx beamforming with zero-forcing precoding and Rx combining in the SI-channel null space to enable simultaneous multi-user operation, yielding closed-form solutions within the resulting reduced subspaces.

The proposed concepts are experimentally validated using a 3×5 Tx and Rx Vivaldi antenna array integrated with a Zynq UltraScale+ RFSoC ZCU216 platform. At 3 and 3.5 GHz, the SI-constrained Tx beamformer achieves more than 45 dB of minimum Tx-to-Rx isolation level, while joint Tx–Rx beamforming increases the system isolation to over 80 dB, with only a few dB reduction in Tx gain. In two-beam MU-MIMO operation, the isolation constraint is likewise met while the desired beams and zero-forcing nulls are preserved. The SI-mitigation principle is further demonstrated in a full-duplex frequency-modulated continuous-wave (FMCW) radar operating at 3 GHz, where the coupled SI is reduced by more than 40 dB across the 100 MHz chirp bandwidth, recovering target echoes that remain masked under conventional maximum-gain transmission.

At the antenna level, a symmetry-constrained convolutional neural network surrogate combined with a genetic algorithm synthesizes four-port full-duplex MIMO patch antennas with improved inter-port isolation, reaching up to 36 dB of measured isolation without additional decoupling structures.

Together, these results show that antenna design, array geometry, and beamforming can be treated as a single SI-mitigation problem, reducing the burden on subsequent analog and digital cancellation stages.

Keywords: In-band full-duplex, self-interference mitigation, full-duplex arrays, beamforming, MIMO, antenna isolation, full-duplex radar, machine learning-assisted antenna design.

List of Publications

This thesis is based on the following publications:

[A] **Mustafa Ayebe**, Johan Malmström, Sten E. Gunnarson, Henrik Holter, Marianna Ivashina, Carlo Bencivenni, and Rob Maaskant, "Systematic Self-Interference Mitigation In Full Duplex Antenna Arrays Via Transmit Beamforming". *2023 IEEE Int. Conf. Electromagn. Adv. Appl. (ICEAA), Venice, Italy, 2023.*

[B] **Mustafa Ayebe**, Rob Maaskant, Johan Malmström, Sten E. Gunnarson, Henrik Holter, and Marianna Ivashina, "3D-printed Silver-coated Vivaldi Array With Integrated Coaxial Probe Feeding". *2024 IEEE Int. Symp. Antennas Propag. INC/USNC-URSI Radio Sci. Meeting (AP-S/INC-USNC-URSI), Firenze, Italy, 2024.*

[C] **Mustafa Ayebe**, Rob Maaskant, Sten E. Gunnarson, Johan Malmström, Marianna Ivashina, and Henrik Holter, "Joint Tx-Rx Beamforming for Optimal Gain and Self Interference Mitigation in In-Band Full-Duplex Arrays: Theory, Figures of Merit, and Validation". *IEEE Antennas Wireless Propag. Lett. (2025), Recipient of the IEEE AP-S Acharya Jagadish Chandra Bose Paper Award.*

[D] **Mustafa Ayebe**, et al., "In-Band Full-Duplex Antenna Beamforming and Synchronization for Self-Interference Mitigation: Multi-Tile RFSoC Testbed Design and Deployment". *2025 19th Eur. Conf. Antennas Propag. (EuCAP), Stockholm, Sweden, 2025.*

[E] **Mustafa Ayebe**, Rob Maaskant, Marianna Ivashina, Henrik Holter, and Johan Malmström, "Generative Deep-Learning Design of Single- and Dual-Polarized Four-Port MIMO Antennas for Full-Duplex Communication". *IEEE Antennas Wireless Propag. Lett. (2026).*

[F] **Mustafa Ayebe**, Rob Maaskant, Bo Göransson, and Henrik Holter, "Transmit and Receive Beamforming for In-Band Full-Duplex MU-MIMO under Self-Interference Constraints with Measurement-Based Validation". *IEEE Open J. Antennas Propag. (2026).*

[G] **Mustafa Ayebe**, Rob Maaskant, Marianna Ivashina, Henrik Holter, and Andreas Wikström, "Antenna-level Self-Interference Suppression in Full-Duplex Radar via Transmit Beamforming". *IEEE Antennas Wireless Propag. Lett. (2026).*

[H] **Mustafa Ayebe**, Rob Maaskant, and Marianna Ivashina, "Self-Interference–Constrained Transmit Beamforming in Interleaved and Displaced In-Band Full-Duplex Arrays: Gain and Isolation Trade–Offs". *2026 IEEE Int. Symp. Antennas Propag. USNC-URSI Radio Sci. Meeting (AP-S/URSI), Detroit, MI, USA, 2026.*

Other publications by the author, not included in this thesis, are:

[I] **Mustafa Ayebe**, Rob Maaskant, "Electronic Device And Method In A Radio Network". *Patent no: WO2024170276A1, Aug, 2024.*

[J] **Mustafa Ayebe**, Rob Maaskant, Johan Malmström, Sten E. Gunnarson, Henrik Holter, and Marianna Ivashina, "Evaluation of the Self-Interference Cancellation Limits of Full-Duplex Antenna Arrays Using Zynq UltraScale+ RF System-On-Chip Board". *2024 IEEE Int. Symp. Phased Array Syst. Technol. (ARRAY), Boston, MA, USA, 2024.*

[K] **Mustafa Ayebe**, Rob Maaskant, "Ferrimagnetic Materials for Non-Reciprocal Shared-Aperture Full-Duplex Antennas". *In preparation for submission to an IEEE conference.*

Author Contributions

For all included papers in the thesis (Papers A through H) as well as the related publications not included in the thesis (Papers I, J, and K), **Mustafa Ayebe** served as the primary author responsible for the research, methodology development, hardware implementation, simulation, measurement setup, and drafting of the manuscripts. *Rob Maaskant* acted as the main supervisor, providing oversight and guidance on the research direction. All other co-authors provided contributions limited to technical discussions, feedback, and review of the papers.

Acknowledgement

First and foremost, I would like to express my sincere gratitude to my supervisor, Prof. Rob Maaskant, for his continuous support, guidance, and encouragement throughout my doctoral studies. His constructive feedback, insightful discussions, and creative ideas have been invaluable to my research and to my development as a researcher. I am also deeply grateful to Prof. Marianna Ivashina for her valuable academic advice, encouragement, and the expertise she has generously shared throughout this journey.

I would like to thank all the members of the Antenna Systems Group for creating a friendly, supportive, and inspiring research environment. A special thanks goes to Teanette van der Spuy, with whom I have shared both an office and a supervisor, for her friendship, support, and encouragement throughout these years. I am also grateful to Usman Shehryar, Charitha Madapathage Don, Merna Tanbkji, and Furkan Keskin for their friendship, encouragement, and the many good memories we have shared during my time at Chalmers. Having you around made this journey more enjoyable and memorable.

I am also grateful to the colleagues and industry partners involved in the DIGIARRAY team, especially Henrik Holter, Sten Gunnarson, Johan Malmström, and Andreas Wikström. I appreciate the valuable discussions, technical feedback, and support that contributed to this work. I would also like to acknowledge the support of the WiTECH Centre (DIGIARRAY project), which is financed by VINNOVA, Ericsson, Saab, and Chalmers.

I would like to extend my deepest gratitude to my family for their unconditional love, patience, and support throughout this journey. Despite the distance, they have always been there for me, encouraging me through the difficult moments and sharing in the happy ones.

Finally, my most heartfelt thanks go to my wife, Zehra, for her love, patience, understanding, and unwavering support throughout these years. She has shared not only the happy moments but also the challenges, uncertainties, and long days that came with this journey. Her presence, encouragement, and belief in me have meant more than I can express in words. Zehra, thank you for being by my side throughout this journey.

Acronyms

IBFD:	In-Band Full-Duplex
SI:	Self-Interference
MIMO:	Multiple Input Multiple Output
FMCW:	Frequency-Modulated Continuous-Wave
ZF:	Zero-Forcing
PA:	Power Amplifier
LNA:	Low Noise Amplifier
Tx:	Transmit
TxGAIN:	Transmit Array Gain
EIRP:	Effective Isotropic Radiated Power
maxTxGain:	Conventional maximum-gain beamformer
Rx:	Receive
RxGAIN:	Receive Array Gain
MRC:	Maximal Ratio Combining
UE:	User Equipment
$\mathbf{S}^{\mathrm{Rx,Tx}}$:	Tx-to-Rx Coupling Matrix
$\mathrm{ISO}^{\mathrm{Rx,Tx}}$:	Receiver array isolation
$\mathrm{ISO}_m^{\mathrm{Rx,Tx}}$:	Isolation of receiver element, m
$\mathrm{ISO}^{\mathrm{sys}}$:	In-band full-duplex system isolation
$\kappa^{\mathrm{Rx,Tx}}$:	Receiver array isolation threshold
κ^{sys}:	In-band full-duplex system isolation threshold
RFSoC:	Radio Frequency System-on-Chip
MTS:	Multi Tile Synchronization
ML:	Machine Learning
CNN:	Convolutional Neural Network

Contents

Abstract i

List of Publications iii

Author Contributions iv

Acknowledgement v

Acronyms vii

I Overview 1

1 Introduction 3
- 1.1 Background on Full-Duplex Communication and Radar . . . 4
  - Opportunities and Applications . . . 4
  - Self-Interference as the Fundamental Challenge . . . 5
- 1.2 Existing Full-Duplex Mitigation Techniques . . . 6
  - Propagation Domain . . . 7
  - Analog-Circuit Domain . . . 9
  - Digital Domain . . . 10
  - Hybrid Approaches . . . 11
- 1.3 Research Objectives and Contributions . . . 12
- 1.4 Thesis Organization . . . 13

2 IBFD Antenna Array System Framework and Beamforming Approach 15
- 2.1 Non-Shared Aperture IBFD System Framework . . . 15
  - Operating Principle and Coupling Mechanisms . . . 15
  - Radiated Power and Realized Gain . . . 18
  - Isolation Definitions . . . 19
- 2.2 Proposed Beamforming Approach . . . 19
  - Rx Array Isolation Control . . . 19
  - SU-MIMO IBFD Architecture: Beamforming Approach . . . 20

MU-MIMO IBFD Architecture: Beamforming Approach . . . 21
2.3 Proof of Concept: Performance Evaluation . . . 23
SU-MIMO IBFD Performance . . . 23
MU-MIMO IBFD Performance . . . 26

3 Integrated IBFD Testbed: Design and Experimental Validation 29
3.1 Integrated IBFD Testbed and Measurement Methodology . . . 29
Tx–Rx Antenna Array Design . . . 30
The RFSoC ZCU216 Platform . . . 31
IBFD Measurement Architecture . . . 32
3.2 IBFD Validation Results and Discussion . . . 34
SU-MIMO IBFD Validation . . . 34
MU-MIMO IBFD Validation . . . 36
3.3 Full-Duplex Radar Validation Results . . . 37
Radar Measurement Configuration and SI Mitigation . . . 39
FMCW Target Detection . . . 40
3.4 Chapter Summary . . . 42

4 Machine-Learning-Assisted Synthesis of Full-Duplex MIMO Antennas 43
4.1 Symmetry-Constrained Antenna Representation . . . 43
4.2 Surrogate Model . . . 44
4.3 Generative Antenna Optimization . . . 45
4.4 Validation . . . 45
4.5 Chapter Remarks . . . 45

5 Summary of included papers 47
5.1 Paper A . . . 47
5.2 Paper B . . . 47
5.3 Paper C . . . 48
5.4 Paper D . . . 48
5.5 Paper E . . . 48
5.6 Paper F . . . 49
5.7 Paper G . . . 49
5.8 Paper H . . . 49

6 Concluding Remarks and Future Research Directions 51

References 53

II Papers 59

A Self-Interference Mitigation In Full Duplex Antenna Arrays A1
1 Introduction . . . A3
2 Array Model and Definitions . . . A5
Maximum Gain Beamformer . . . A5
Minimum TX-RX Isolation Constraint . . . A7
Min. TX-RX Isolation + Max. TX Gain Constraints . . . A8
3 Performance Evaluation . . . A8

4 Conclusion . . . A11
References . . . A11

B Vivaldi Antenna Element Design **B1**
1 Introduction . . . B3
2 Antenna Structure and Simulation . . . B3
3 Validation for 1-D Array . . . B5
4 Conclusion . . . B6
References . . . B6

C Joint Tx-Rx Beamforming for Optimal Gain and Self-Interference Mitigation **C1**
1 Introduction . . . C3
2 In-Band Full-Duplex antenna system model . . . C4
3 Proposed Beamforming Method . . . C5
4 Analysis and Validation Results . . . C6
IBFD system case study and measurement setup . . . C6
Results and Discussion . . . C8
5 Conclusion . . . C9
1 Proof on Minimum ISO for Subspace Beamformer . . . C9
2 RX Beamformer . . . C11
References . . . C11

D In-Band Full-Duplex Communication and Sensing Testbed **D1**
1 Introduction . . . D3
2 The RFSoC ZCU216 . . . D4
3 DAC and ADC Clock Synchronization . . . D4
4 IBFD Testbed and Beamforming Algorithm . . . D5
IBFD Testbed Configuration . . . D6
Tx and Rx Beamforming Algorithm . . . D6
The Measurement Procedure . . . D7
5 Performance Evaluation . . . D8
Synchronization Results . . . D8
6 Conclusion . . . D9
1 Continuous Waveform Generation for DAC . . . D9
References . . . D10

E Machine Learning-Assisted Antenna Design **E1**
1 Introduction . . . E3
2 Symmetric Antenna Modeling and Synthesis . . . E5
Pixel-Based Symmetric Antenna Representation . . . E5
Dataset Generation and Neural Network Modeling . . . E5
3 Validation . . . E8
Discussion . . . E9
Relative Evaluation with Reported Works . . . E10
4 Conclusion . . . E11
References . . . E11

F Beamforming for In-Band Full-Duplex Multi-User MIMO **F1**
1 Introduction . . . F3

2 System Model and Definitions . . . F5
Operating Principle and Coupling Mechanisms . . . F5
Definition of Coupling Matrices Between BS and UEs . . . F7
Radiated Power and Realized Gain . . . F8
Isolation Definitions . . . F9
3 Beamforming Problem Formulation . . . F9
ZFTx Beamforming with SI Control . . . F9
ZFRx-Beamforming with Residual SI Mitigation . . . F10
4 Proof of Concept: Performance Evaluation . . . F12
Sensitivity of Array Isolation to Excitation and Coupling Errors . . . F14
5 Case Study and Validation Results . . . F15
Measurement Setup and Case Study Description . . . F15
Results and Discussion . . . F17
Practical Considerations . . . F18
6 Conclusion . . . F19
References . . . F19

G Full-Duplex Radar **G1**
1 Introduction . . . G3
2 Full-Duplex Radar System Model . . . G4
Signal Model . . . G4
Echo and SI Channel Descriptions . . . G5
3 Beamforming Approach . . . G7
4 Experimental Validation . . . G8
Testbed and Measurement Procedure . . . G8
SI Suppression . . . G9
FMCW Target Detection . . . G10
5 Conclusion . . . G10
References . . . G12

H Interleaved and Displaced In-Band Full-Duplex Arrays **H1**
1 Introduction . . . H3
2 Antenna Structure and Simulation Setup . . . H4
3 Results and Discussion . . . H5
4 Design Implications for Fixed-Aperture Tx/Rx Arrays . . . H7
5 Conclusion . . . H8
References . . . H8

Part I

Overview

CHAPTER 1

Introduction

Wireless communication and radar systems have traditionally separated transmission and reception in time or frequency to limit transmitter-to-receiver interference. In wireless communication, this separation is achieved through time-division duplexing (TDD), in which transmission and reception occupy different time intervals, or frequency-division duplexing (FDD), in which they operate over separate frequency bands. Similarly, conventional radar systems typically alternate between transmitting a waveform and receiving the corresponding target echoes. Although these approaches effectively limit direct transmitter-to-receiver interference, they constrain the simultaneous use of available time–frequency resources and, in some applications, interrupt continuous observation of the environment. The continuing demand for higher data rates, lower latency, more efficient spectrum utilization, and continuous sensing has consequently driven interest in full-duplex wireless communication and radar systems [1], [2], [3], [4].

In-band full-duplex (IBFD) operation enables simultaneous transmission and reception over the same frequency band and, typically, within the same time–frequency resource. In communication systems, this capability can improve spectral efficiency compared with half-duplex operation [5]. In radar systems, it allows target echoes to be received while the transmitter remains active, supporting continuous observation in suitable radar architectures. Furthermore, IBFD can facilitate the integration of sensing and communication functions within a common radio platform [4], [6]. However, simultaneous transmission and reception introduce a fundamental challenge: self-interference (SI), which arises when the transmitted signal couples into the receive (Rx) chain. In communication systems, SI can overwhelm the desired signal arriving from a remote transmitter, whereas in radar systems, direct transmitter (Tx) leakage and unwanted reflections can mask weak target echoes and degrade detection performance.

This thesis investigates SI mitigation from a spatially integrated perspective, treating the antenna array not merely as an interface between the radio frequency (RF) transceiver and the propagation environment, but also as an active resource for interference management. Antenna topology and array geometry are investigated as means of establishing Tx-to-Rx isolation, while spatial beamforming provides an additional mechanism for controlling SI. Spatial combining and, where necessary, RF and digital cancellation can then be employed

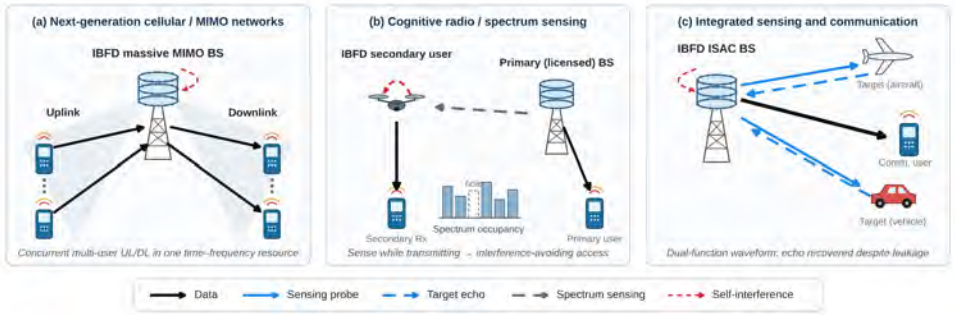


Figure 1.1: Examples of IBFD applications. (a) Cellular/MIMO networks, where an IBFD base station (BS) serves multiple uplink and downlink users concurrently and must suppress SI. (b) Cognitive radio, where an IBFD secondary user senses the licensed band while transmitting, enabling interference-avoiding spectrum access. (c) ISAC, where a dual-function waveform supports data transmission and the reception of target echoes. Figure generated with the assistance of Claude Sonnet 5.5 [9].

to suppress the remaining interference. This perspective provides the basis for the antenna-, beamforming-, and hardware-level investigations developed throughout this thesis.

1.1 Background on Full-Duplex Communication and Radar

In communication systems, IBFD removes the resource separation inherent to TDD and FDD. In radar systems, it allows target echoes to be observed while the transmitted waveform remains active. This capability is particularly relevant to continuous-wave (CW) radar architectures, in which transmitted and received signals coexist and are processed to estimate target parameters such as range and radial velocity. Because the receiver listens while the transmitter is on, CW radar avoids the idle receive interval of pulsed operation, but the Tx and Rx apertures must then be isolated from one another.

The strong coupling between the Tx and Rx chains is the main obstacle to practical IBFD operation. In communication systems, the SI signal can substantially exceed the signal received from a remote user. In radar systems, the target echo is attenuated by propagation loss and target reflectivity, whereas in CW radar the leakage produces a dominant near-zero-range response that elevates the effective detection floor and complicates the detection of nearby targets. Effective SI mitigation is therefore essential to exploit the potential benefits of full-duplex operation. This requires techniques operating across the propagation, analog/RF, and digital domains [7], [8], which are reviewed in Section 1.2.

Opportunities and Applications

Beyond its potential to improve spectral efficiency, IBFD enables wireless platforms to perform multiple functions concurrently within the same time–frequency resource. This capability is particularly valuable in applications requiring simultaneous communication, sensing, spectrum access, or energy transfer. Figure 1.1 illustrates three representative examples, and the applicability of IBFD extends across a broader range of wireless platforms:

- **Next-generation cellular and MIMO networks:** IBFD can support simultaneous uplink and downlink transmission, potentially increasing the capacity of multi-user (MU) base stations. The achievable gain depends on SI suppression and on

the management of multi-user, inter-user (cross-link), and inter-cell interference [10]. In large-scale multiple-input multiple-output (MIMO) systems, spatial beamforming provides degrees of freedom (DoF) for MU transmission and reception while offering additional opportunities for SI suppression [5].

- **Cognitive radio and spectrum sensing:** Full-duplex radios can monitor the surrounding spectrum while maintaining transmission, enabling more dynamic spectrum access, better knowledge of spectral occupancy, and interference-avoiding operation with respect to licensed users [2].
- **Integrated sensing and communication:** IBFD is attractive for integrated sensing and communication (ISAC), also referred to as joint communication and sensing, where a common radio platform supports communication and environmental sensing concurrently [11]. Depending on the architecture, the receiver may process target echoes, signals from other communication nodes, or both. This introduces additional interference-management requirements because the desired sensing and communication signals must be recovered in the presence of local leakage and potentially overlapping interference [4], [6], [12]. Such capabilities are relevant to autonomous systems, intelligent transportation, and smart infrastructure.
- **Wireless power transfer:** An IBFD access point or relay can transfer energy to energy-harvesting devices while receiving their data over the same resources, as studied in full-duplex wireless-powered communication networks [2], [13]. This is relevant to power-limited deployments, although the strong transmitted energy signal makes SI suppression particularly important.
- **Internet of Things and edge systems:** Full-duplex transceivers can improve bidirectional communication efficiency in dense and latency-sensitive networks. However, compact device architectures constrain the physical separation between Tx and Rx antennas, increasing the importance of effective SI mitigation.
- **Non-terrestrial and satellite communication systems:** Full-duplex operation can enable more flexible spectrum utilization and simultaneous operation of communication links in satellite and other non-terrestrial architectures. The large difference between transmitted and received power levels makes SI cancellation especially demanding, so feasibility depends on the specific use case [14].

These applications illustrate the potential benefits of IBFD operation, while highlighting the importance of effective SI mitigation for practical implementation.

Self-Interference as the Fundamental Challenge

The transmitted signal in an IBFD system can couple into the receiver through multiple physical mechanisms. These include direct Tx-to-Rx antenna coupling, near-field interactions, surface-wave coupling, reflections and scattering from the surrounding environment, and leakage through the RF transceiver circuitry. Practical RF hardware also introduces nonidealities, such as power-amplifier (PA) nonlinearities, oscillator phase noise, and digital-to-analog converter (DAC) and analog-to-digital converter (ADC) limitations, which can affect SI cancellation performance [15].

The severity of SI depends on the propagation environment, antenna configuration, transmitted power, and receiver architecture. In communication systems, the difference between

transmitted leakage and the desired received signal can approach 110 dB in representative scenarios, imposing stringent requirements on receiver dynamic range and linearity [16]. In radar systems, the required suppression depends on the transmitted power, target characteristics, waveform, receiver architecture, and detection requirements. Because the desired echo is a delayed and attenuated version of the transmitted waveform, even moderate Tx leakage can mask weak target echoes, particularly at short ranges. SI mitigation must therefore suppress unwanted coupling without indiscriminately removing the delayed and Doppler-shifted target information required for sensing. In both communication and radar applications, the interference must also be reduced sufficiently to avoid low-noise amplifier (LNA) saturation and permit reliable recovery of the desired signal.

Several characteristics make SI mitigation particularly challenging:

- **Strong and spatially structured coupling:** In an antenna array, the received SI results from the coherent superposition of coupling contributions from the Tx elements. Consequently, SI cannot generally be characterized adequately by considering individual antenna pairs independently. Instead, a coupling matrix describes how the excitation of the Tx array affects the signals induced across the Rx array. This matrix provides a useful representation of the aggregate coupling between the arrays and can support the design of spatial SI mitigation techniques.

- **Dynamic electromagnetic environment:** Reflections and scattering from nearby objects can modify the effective coupling response. Motion, environmental changes, and frequency variation can therefore alter the SI channel [8]. In communication systems, such variations can reduce the accuracy of SI-channel estimation and cancellation. In radar systems, environmental reflections can also contribute clutter whose delay and Doppler characteristics overlap with those of the target of interest.

- **Compact antenna arrangements:** Limited physical separation between Tx and Rx apertures can increase coupling and restrict the available spatial DoF for interference suppression. This issue is particularly relevant to compact MIMO, mobile, and IoT platforms [17]. Although compact arrays are attractive for reducing system size and supporting spatial coverage, their geometry can result in strong mutual coupling. Antenna topology and array arrangement therefore play an important role in determining the achievable intrinsic isolation.

- **Trade-offs across cancellation domains:** SI mitigation typically combines propagation, analog, and digital domain techniques, each with inherent trade-offs. Propagation domain suppression exploits antenna placement, radiation patterns, and other electromagnetic properties to reduce coupling before the signal reaches the receiver. Analog cancellation (pre-ADC) helps prevent receiver saturation but can be power-hungry and difficult to scale to large arrays, while digital cancellation (post-ADC) offers flexibility but requires accurate interference modeling and may introduce latency [18], [19]. In radar systems, cancellation must also preserve the amplitude and phase information required for target detection and parameter estimation.

These challenges motivate coordinated SI mitigation across the antenna, RF, and signal-processing domains, with antenna-level isolation as the first line of defense.

1.2 Existing Full-Duplex Mitigation Techniques

Practical IBFD systems generally employ multiple layers of SI suppression, categorized according to where the cancellation takes place: the propagation domain, the analog-circuit

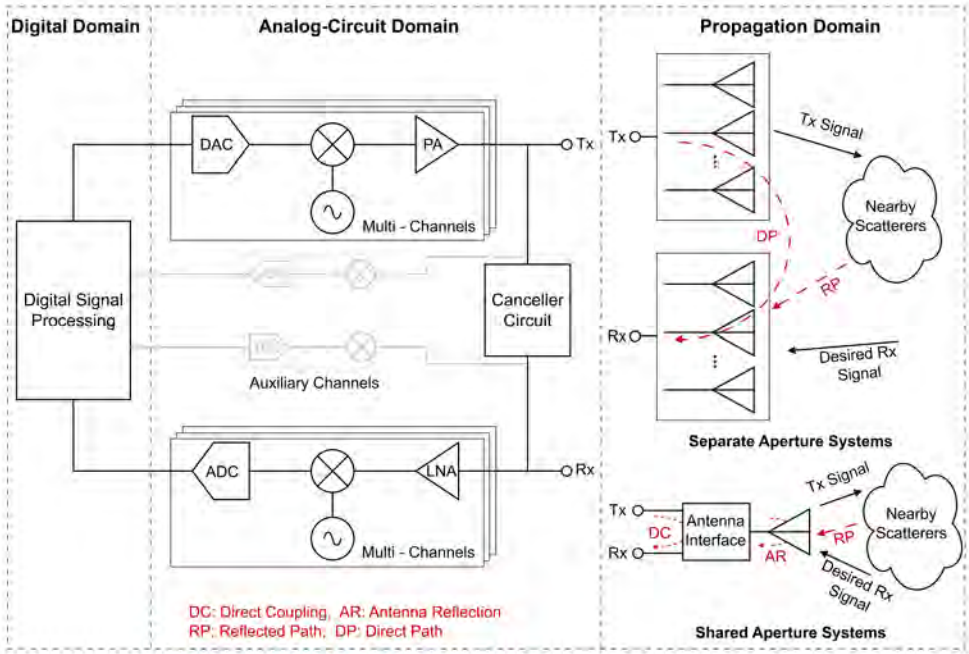


Figure 1.2: Representative IBFD transceiver architecture, highlighting propagation-, analog-circuit-, and digital-domain SI mitigation techniques.

domain, and the digital domain. Figure 1.2 illustrates a representative IBFD transceiver architecture and the interaction between these domains.

In the propagation domain, the system architecture accommodates either a shared or non-shared aperture. In spatially separated setups, SI is dominated by direct inter-array coupling, whereas shared-aperture designs suffer from internal aperture reflections and severe mutual coupling. In both cases, these direct paths combine with dynamic environmental reflections from nearby scatterers to create complex, time-varying interference channels.

The analog domain encompasses the RF and analog circuitry between the antenna interfaces and the digital conversion stages. On the Tx side, the signal chain includes a multi-channel DAC, frequency upconversion via a mixer, PA, and the Tx antenna. The receive path follows a complementary structure: the Rx antenna feeds into an LNA, followed by frequency downconversion, multi-channel processing, and an ADC. As shown in Figure 1.2, a cancellation circuit is integrated between the Tx and Rx paths. This canceller operates at the propagation frequency and is placed after the PA. In alternative architectures, auxiliary channels are used to facilitate SIC in both the analog and digital domains.

Lastly, the digital domain comprises a digital signal processing unit that manages all digital SI cancellation procedures.

Propagation Domain

Propagation-domain techniques aim to minimize direct-path coupling between the Tx and Rx antennas and can be classified into passive, active, and antenna-interface techniques.

Passive techniques rely on fixed antenna configurations or electromagnetic structures

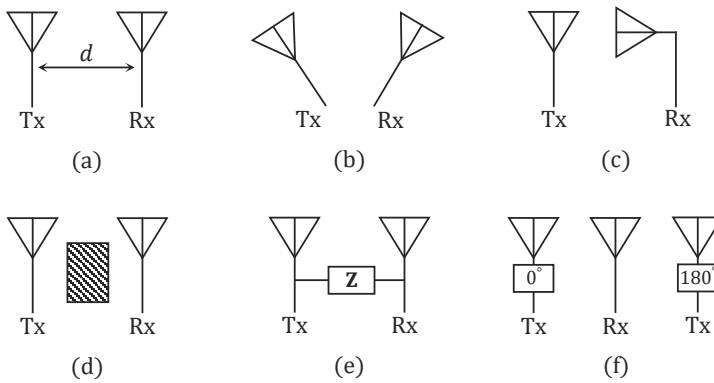


Figure 1.3: Propagation domain passive techniques: (a) physical separation, (b) spatial separation, (c) orthogonal polarization, (d) surface treatments, (e) coupling networks, and (f) phase control.

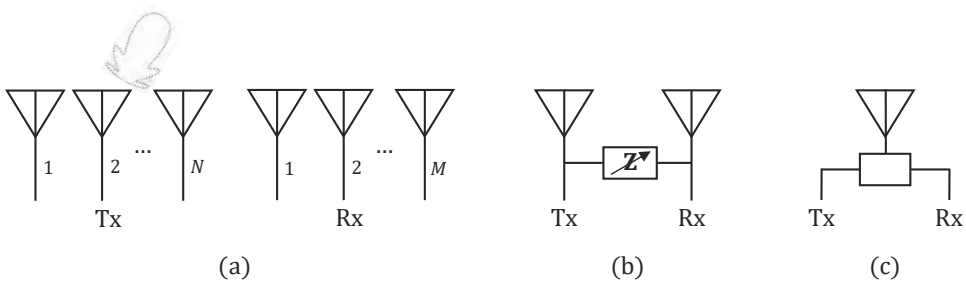


Figure 1.4: Propagation domain active techniques: (a) transmit beamforming and (b) tunable coupling network, and (c) antenna-interface techniques.

and therefore do not require real-time adaptation. Common techniques include:

- *Antenna & Directional separation:* Physical distance, d, and spatial orientation between antennas (see Figures 1.3(a)&(b)) increase path loss or reduce radiation pattern overlap to attenuate SI [20].
- *Polarization Orthogonality:* Tx and Rx antennas operate on orthogonal polarizations to naturally minimize cross-coupling [21] as shown in Figure 1.3(c).
- *Surface Treatments:* Absorbers, reflective structures, and high-impedance surfaces, such as metasurfaces, are deployed between antennas as presented in Figure 1.3(d) to suppress surface currents and unwanted coupling [22], [23].
- *Coupling Networks:* Fixed impedance networks (resistors, capacitors, or inductors) shown in Figure 1.3(e) inserted between antennas modify electromagnetic paths to reduce coupling [24], [25].
- *Phase Control:* Antenna configurations introduce fixed phase shifts to create near-field nulls at the receiver. Examples include antiphase setups in Figure 1.3(f) and circular-mode techniques using Butler matrices for omnidirectional coverage [26], [27].

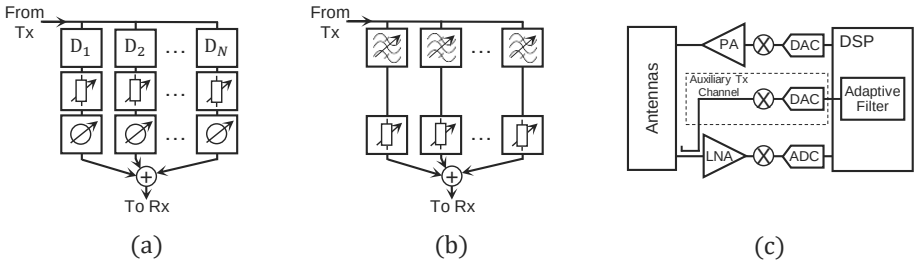


Figure 1.5: Analog domain techniques (redrawn from Fig. 6 in [7]): (a) time-domain approaches, (b) frequency-domain approaches, and (c) digitally assisted approaches.

Active techniques employ real-time tunable elements to suppress interference adaptively, better suiting dynamic environments:

- *Transmit Beamforming:* By adjusting the amplitude and phase of multiple Tx antennas, the near-field radiation pattern of a Tx array can be shaped to create a null at the receive antenna port, thereby reducing SI [28], [29], as shown in Figure 1.4(a).
- *Tunable Coupling Networks:* Variable-impedance components, such as varactors, are tuned to adjust the coupling between the Tx and Rx antennas and minimize SI [30], as illustrated in Figure 1.4(b).

Antenna interface techniques employ balanced duplexers, circulators, and related RF components to suppress Tx-to-Rx leakage at the antenna interface [31], as illustrated in Figure 1.4(c). Balanced duplexers rely on cancellation within balanced networks, whereas circulators exploit nonreciprocal signal routing to provide Tx–Rx isolation, with performance governed primarily by isolation, insertion loss, bandwidth, and power handling.

Analog-Circuit Domain

Analog SI cancellation is implemented within the RF front-end and is categorized based on where the cancellation occurs along the receive chain—typically at RF, intermediate frequency (IF), or baseband (BB). The primary goal is to reduce the strength of the SI signal to avoid saturating the LNA and downstream receiver components [32], [33]. For narrowband operation, the SI channel can often be represented using simple gain-and-delay models [17], [34], whereas wideband operation requires a more detailed representation of its frequency-selective response and may benefit from digital assistance [35]. The achievable cancellation is limited by channel-estimation errors, calibration accuracy, and hardware nonidealities [34]. These cancellation techniques can be classified into three approaches.

Time-domain cancellers use multiple delayed replicas of the transmit signal with independently adjustable amplitude and phase to approximate the SI channel response (Figure 1.5(a)). They can provide broadband cancellation but require multiple analog delay paths, increasing hardware complexity as the channel response becomes more complex. RF and IF implementations have been demonstrated [36], [37].

Frequency-domain cancellers, shown in Figure 1.5(b), use tunable narrowband filters and variable attenuators to synthesize the SI spectrum. By eliminating delay elements, they simplify integrated circuit implementation and enable RF cancellation before the LNA [38].

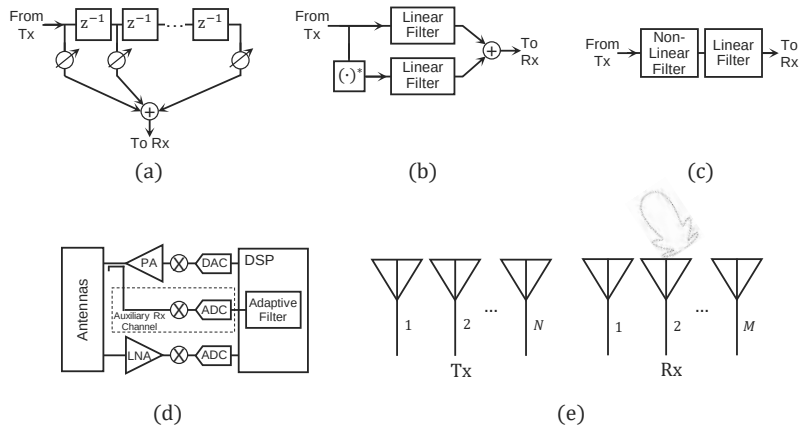


Figure 1.6: Digital domain techniques (adapted from Fig. 7 in [7]): (a) linear model, (b) widely linear model, (c) nonlinear model, (d) reference-based model, and (e) receive beamforming.

Digitally assisted cancellers generate the cancellation waveform digitally, convert it to the analog domain, and inject it into the receiver path as depicted in Figure 1.5(c). This architecture provides a large number of effective cancellation paths and flexible adaptation, but requires an additional signal path and may not capture transmitter noise and nonlinear distortion present in the actual transmitted waveform [39].

These architectures provide complementary trade-offs in hardware complexity, bandwidth, and cancellation capability and are typically combined with propagation- and digital-domain techniques to achieve the required overall SI suppression.

Digital Domain

Digital-domain techniques are implemented in the digital baseband (BB), providing flexible SI cancellation without hardware modification. As depicted in Figure 1.6, these techniques can be broadly categorized into channel modeling and receive beamforming.

Channel modeling techniques generate a digital replica of the SI for subtraction after the ADC, with cancellation performance determined by the accuracy of the interference-channel model. Depending on the system characteristics, linear finite impulse response models (Figure 1.6(a)) can reconstruct SI from the transmitted signal [40], while widely linear models, illustrated in Figure 1.6(b), account for image components caused by in-phase/quadrature imbalance [41]. Nonlinear models, shown in Figure 1.6(c), extend linear models by incorporating estimates of nonlinear transmit-signal distortions, primarily caused by the PA but also by other components in the transmit chain. These distortions become more pronounced as the output power increases [42]. Alternatively, reference-based models use a measured transmit signal with an auxiliary Rx channel, as shown for the PA output in Figure 1.6(d), that captures practical hardware impairments [43].

Receive beamforming techniques, illustrated in Figure 1.6(e), exploit multiple Rx antennas, channels, and spatial DoF to suppress SI while preserving the desired signal. After ADC conversion, the received signals are digitally weighted and combined to steer spatial nulls toward the interference source, analogous to Tx beamforming [44].

While digital SI cancellation offers high adaptability, its effectiveness depends on sufficient suppression in the propagation and analog domains. Its performance is ultimately limited by the ADC dynamic range: post-ADC processing cannot recover information lost to LNA compression or ADC saturation, so strong SI must be suppressed before the receiver reaches its operating limits.

Hybrid Approaches

The limitations of individual SI mitigation techniques have motivated hybrid architectures that distribute interference suppression across multiple domains. Propagation-domain techniques provide initial isolation, analog cancellation further reduces SI before the receiver front end, and digital cancellation suppresses the residual interference after ADC conversion [33], [35]. By combining these stages, overall SI suppression exceeding 110 dB has been demonstrated in practical IBFD systems [35].

Despite their effectiveness, hybrid architectures increase hardware, processing, power, and calibration requirements. These challenges become more pronounced in large-scale MIMO systems, where the number of cancellation paths can grow with the number of antenna elements. Moreover, their performance may degrade as the SI channel changes with the antenna configuration and electromagnetic environment.

These limitations motivate the use of the spatial DoF of MIMO arrays as an additional SI mitigation mechanism. By controlling the Tx excitation, the transmitted radiation can be shaped to reduce the SI coupled into the Rx array before the receiver front end, without dedicated RF cancellation paths, while maintaining useful radiation toward the intended communication user or radar coverage region.

Beamforming-Based Approaches

Beamforming-based approaches exploit the spatial DoF of MIMO arrays to control the transmitted and received spatial fields. Depending on the architecture, beamforming can be applied at the Tx side, Rx side, or jointly at both sides.

Consider an IBFD system with N Tx antennas and M Rx antennas. The electromagnetic coupling between the arrays can be represented by the Tx-to-Rx coupling matrix $\mathbf{S}^{\mathrm{Rx,Tx}} \in \mathbb{C}^{M\times N}$. Tx beamforming can then be designed such that the transmitted signal lies in the null space of coupling matrix, thereby suppressing the SI coupled into the Rx array. When $N > M$, the SI channel matrix has at least $N - M$ zero singular values, with corresponding right-singular vectors providing spatial DoF for null-space projection [45].

To enhance full-duplex data rates, iterative beamforming strategies have been proposed for phased array systems [46]. This approach optimizes the Tx and Rx beamformer weights to achieve wideband SI cancellation purely in the spatial domain. It reduces the need for specialized RF cancellation circuitry while preserving both Tx and Rx gain.

Table 1.1 summarizes the performance of measured IBFD systems employing adaptive beamforming techniques. The table highlights key parameters, including the number of Tx and Rx antennas, beamforming methods, additional cancellation techniques, Effective Isotropic Radiated Power (EIRP), and total SI suppression achieved. Beamforming alone can provide at least 62 dB of SI cancellation, as demonstrated in [28], [29]. However, several systems combine beamforming with propagation, analog, and digital cancellation to achieve higher suppression levels, reaching 140.5 dB in advanced configurations [47].

Despite the demonstrated potential of beamforming-based SI mitigation, several chal-

Table 1.1: Performance evaluation of measured IBFD systems using adaptive beamforming methods.

Ref	# of Tx, Rx elements	Beamforming method	Additional SIC scheme	f_c (GHz)	EIRP (dBm)	Total SIC (dB)
[28]	2, 1	Hybrid Tx	None	3.3	3.0	62.0
[29]	2, 1	Digital Tx	None	3	0.0^{+}	63.0
[47]	4, 4	Digital Tx and Rx	Digital	2.45	44.8	140.5
[48]	36, 36	Digital Tx	Digital	2.4	0.0^{+}	87.0
[49]	8, 1	Hybrid Tx	Prop. & Analog	2.45	22.7	96.0
[50]	4, 4	Digital Tx	Digital	2.4	10.0	76.0
[51]	2, 4	Digital Tx and Rx	None	4.5	12.0	97.0
[52]	8, 8^{*}	Analog Tx and Rx	Prop. & Digital	0.73	16.5	100.0

$^{+}$ Antenna array gain was not reported, so it was not included in the EIRP calculation.
* Circulators enabled the sharing of antenna elements for both transmission and reception.

lenges remain for practical IBFD systems:

- **Dependence on coupling-channel knowledge:** Spatial SI suppression relies on an accurate representation of the Tx-to-Rx coupling response. In practice, the coupling matrix is obtained via simulation or measurement and is affected by estimation errors, calibration imperfections, frequency variations, and environmental changes. Such inaccuracies can result in residual SI and limit the achievable suppression.

- **Trade-off between SI suppression and communication performance:** Exact null-space projection can suppress the modeled SI when a nontrivial null space exists, but the corresponding spatial DoF are then unavailable for desired transmission. More stringent SI suppression can therefore reduce Tx array gain, distort the desired beam pattern, or limit spatial multiplexing.

- **Receiver protection and practical SI constraints:** The required SI suppression is set by the interference tolerance of the receiver front end, as discussed in the digital-domain review above. Sufficient SI reduction must be achieved before the receiver reaches its operating limits, while avoiding unnecessarily stringent constraints that consume useful spatial DoF.

- **Joint Tx–Rx and multi-user requirements:** In practical MIMO and MU-MIMO systems, SI suppression must coexist with the spatial constraints of desired communication channels. Joint Tx–Rx designs must simultaneously provide useful radiation, limit coupling toward the Rx array, preserve desired signals, and suppress residual SI. Such formulations may require iterative optimization and repeated channel updates, increasing computational complexity and limiting real-time applicability.

Together, these challenges motivate a shift from exact SI nulling to the SI-constrained spatial optimization adopted in this thesis, which is introduced in the next section.

1.3 Research Objectives and Contributions

The discussion above shows that practical SI mitigation requires more than a single cancellation mechanism. The central objective of this thesis is therefore to develop and experimentally validate an integrated antenna-system approach to SI mitigation in IBFD systems.

The research is built around the principle of *SI-constrained spatial optimization*: rather than requiring complete elimination of the Tx–Rx coupling, the coupled SI power is constrained to a level compatible with receiver operation, while the remaining spatial DoF are

exploited for useful transmission and reception. The Tx–Rx coupling matrix is incorporated directly into the beamforming problem, so that the available DoF are used efficiently, and only the SI suppression required for system operation is enforced.

The main contributions of the thesis are summarized as follows:

- **Beamforming formulation:** A multi-port framework is developed to represent Tx–Rx coupling and the resulting SI power using scattering parameters and power-wave quantities. Based on this framework, Tx beamforming is formulated to maximize useful radiation subject to a constraint on the coupled SI power, moving beyond complete SI nulling toward a controlled gain–isolation trade-off [53]. The framework is further extended to joint Tx–Rx spatial processing, where Tx beamforming provides receiver protection and Rx combining suppresses residual SI [54]. In parallel, Tx–Rx array geometries, including interleaved and vertically displaced configurations, are investigated in terms of their impact on the coupling subspace, available spatial DoF, and gain–isolation trade-off [55].

- **MU-MIMO extension:** The spatial beamforming framework is extended to IBFD MU-MIMO, where SI suppression must coexist with the spatial requirements of simultaneous MU transmission and reception. Closed-form Tx and Rx beamforming solutions based on measured coupling and communication channels are developed and experimentally validated using strongly coupled Vivaldi arrays [56].

- **Experimental full-duplex platform:** A practical IBFD communication and sensing testbed is developed based on a Radio Frequency system on chip (RFSoC) evaluation board integrated with 3×5 Tx and Rx Vivaldi antenna arrays [57] for experimental validation. The platform supports multi-channel waveform generation, coherent synchronization, calibration, digital beamforming, and SI measurements [29], [58].

- **Full-duplex radar:** The antenna-level SI suppression principle is extended from communication to full-duplex frequency-modulated continuous-wave (FMCW) radar. By constraining the Tx excitation to a low-coupling spatial subspace, strong near-zero-range SI is suppressed while preserving useful Tx radiation, enabling target echoes to be detected in the presence of strong direct leakage [59].

- **Machine-learning-assisted antenna synthesis:** SI mitigation is further addressed at the antenna-design level through a machine-learning-assisted synthesis framework for compact four-port MIMO patch antennas. A symmetry-constrained pixel representation, a multi-task convolutional neural network surrogate, and a binary genetic algorithm are combined to search a large topology space for designs with improved impedance matching and inter-port isolation [60].

Together, these contributions establish a system-level approach in which antenna design and geometry determine the intrinsic coupling environment, while Tx and Rx spatial processing exploit the available DoF to satisfy the required SI constraint and preserve useful system performance. The resulting concepts are validated experimentally and extended from communication to sensing applications.

1.4 Thesis Organization

The remainder of the thesis presents the theoretical development, experimental validation, and antenna-level extensions of the proposed approach to SI mitigation.

- **Chapter 2** develops the theoretical framework for non-shared-aperture IBFD antenna arrays. It introduces the multi-port system representation, power-wave formulation, radiation and realized-gain definitions, and relevant isolation metrics. The chapter then formulates the Tx beamforming and Rx beamforming problems and analyzes the trade-off between SI suppression, spatial DoF, and desired beamforming performance.
- **Chapter 3** presents the experimental realization of the proposed beamforming framework. It describes the RFSoC-based full-duplex testbed, custom Vivaldi antenna arrays, synchronization and calibration procedures, and measurement methodology. The chapter then extends the SI-constrained Tx beamforming approach to full-duplex FMCW radar and experimentally demonstrates SI suppression and target detection.
- **Chapter 4** addresses SI mitigation at the antenna-design level. A machine-learning-assisted methodology is presented for synthesizing compact four-port MIMO antennas with enhanced intrinsic isolation.
- **Chapter 5** provides paper summaries included in this thesis.
- **Chapter 6** concludes the thesis by summarizing the main findings and contributions and discussing directions for future research toward practical IBFD communication and sensing systems.

Overall, the thesis progresses from SI-constrained beamforming to experimental validation in communication and sensing systems, followed by antenna-level optimization. This progression reflects the central premise of the thesis: SI mitigation should be treated as a coordinated antenna-system design problem in which antenna coupling, antenna geometry, spatial DoF, beamforming, and hardware constraints are considered together.

CHAPTER 2

IBFD Antenna Array System Framework and Beamforming Approach

2.1 Non-Shared Aperture IBFD System Framework

A non-shared aperture in-band full-duplex (IBFD) antenna array system is considered, comprising an N-element transmit (Tx) antenna array and an M-element receive (Rx) antenna array, as illustrated in Figure 2.1. Each Tx antenna element is independently driven by a dedicated power amplifier (PA), while each Rx antenna element is connected to a dedicated low-noise amplifier (LNA). The considered framework supports both single-user (SU) and multi-user (MU) multiple-input multiple-output (MIMO) operation through the simultaneous generation of K transmit and receive beams. Here, K denotes the number of simultaneously generated spatial beams, corresponding to the number of served single-antenna user equipments (UEs) in the considered architecture. The case $K = 1$ corresponds to SU-MIMO IBFD operation, whereas $K > 1$ corresponds to MU-MIMO IBFD operation.

Operating Principle and Coupling Mechanisms

The system behavior is described using scattering (S)-parameters and power-wave representations following the formalism introduced in [61]. In this framework, the $\mathbf{a}$-waves denote the incident power waves entering the antenna ports, whereas the $\mathbf{b}$-waves denote the outgoing power waves leaving the ports. The analysis is performed under the self-interference (SI)-dominant assumption, where thermal noise and external interference contributions are neglected for analytical tractability.

From an antenna array perspective, the proposed framework represents a generalized beamforming-based SU/MU-MIMO IBFD architecture, where multiple spatial beams are synthesized through complex excitation control of the Tx and Rx antenna elements. Unlike conventional MIMO formulations based on abstract baseband channel matrices, the considered approach models the physical interactions among the Tx, Rx, and UEs through their corresponding scattering submatrices. Therefore, both the desired communication channels and the SI channel are governed by the underlying electromagnetic coupling mechanisms.

The transmit beamforming (precoding) matrix is defined as

$$\mathbf{W}^{\mathrm{Tx}} = \left[\mathbf{w}_1^{\mathrm{Tx}}, \mathbf{w}_2^{\mathrm{Tx}}, \ldots, \mathbf{w}_K^{\mathrm{Tx}}\right] \quad \in \mathbb{C}^{N \times K}, \tag{2.1}$$

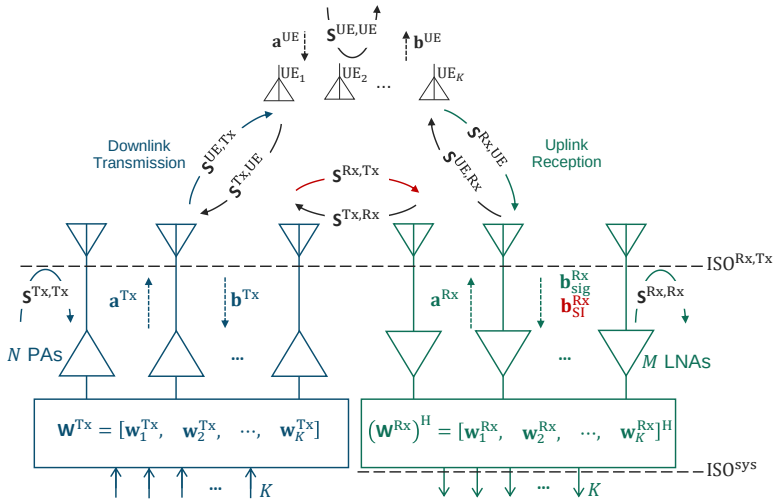


Figure 2.1: Considered non-shared aperture SU/MU-MIMO IBFD beamforming framework comprising an N-element Tx antenna array and an M-element Rx antenna array. The Tx and Rx arrays employ the beamforming matrices $\mathbf{W}^{\mathrm{Tx}}$ and $\mathbf{W}^{\mathrm{Rx}}$, respectively, to synthesize K simultaneous downlink and uplink beams. Owing to IBFD operation, the Rx array is exposed to SI generated by the Tx array through the Tx–to–Rx electromagnetic coupling matrix $\mathbf{S}^{\mathrm{Rx,Tx}}$.

where $\mathbf{w}_k^{\mathrm{Tx}} \in \mathbb{C}^{N\times 1}$ denotes the excitation vector used to synthesize the kth Tx beam. Each vector controls the amplitude and phase distribution across the N Tx antenna elements and satisfies $\|\mathbf{w}_k^{\mathrm{Tx}}\|_2 = 1, \forall k$. After amplification by the PAs, the resulting incident power-wave vector at the Tx ports is denoted by $\mathbf{a}^{\mathrm{Tx}}$. Similarly, the receive beamforming matrix is defined as

$$\mathbf{W}^{\mathrm{Rx}} = \left[\mathbf{w}_1^{\mathrm{Rx}}, \mathbf{w}_2^{\mathrm{Rx}}, \ldots, \mathbf{w}_K^{\mathrm{Rx}}\right] \quad \in \mathbb{C}^{M\times K}, \tag{2.2}$$

where $\mathbf{w}_k^{\mathrm{Rx}}$ represents the unit-norm combining vector associated with the kth Rx beam. The receive combining operation is performed through $(\mathbf{W}^{\mathrm{Rx}})^{\mathrm{H}}$, where $(\cdot)^{\mathrm{H}}$ denotes the Hermitian (conjugate transpose) operator. The corresponding outgoing power-wave vector at the Rx ports is denoted by $\mathbf{b}^{\mathrm{Rx}}$.

The electromagnetic interactions among the Tx array, Rx array, and UEs are described by the overall scattering matrix

$$\underbrace{\begin{bmatrix}\mathbf{b}^{\mathrm{Tx}}\\ \mathbf{b}^{\mathrm{Rx}}\\ \mathbf{b}^{\mathrm{UE}}\end{bmatrix}}_{\mathbf{b}} = \underbrace{\begin{bmatrix}\mathbf{S}^{\mathrm{Tx,Tx}} & \mathbf{S}^{\mathrm{Tx,Rx}} & \mathbf{S}^{\mathrm{Tx,UE}}\\ \mathbf{S}^{\mathrm{Rx,Tx}} & \mathbf{S}^{\mathrm{Rx,Rx}} & \mathbf{S}^{\mathrm{Rx,UE}}\\ \mathbf{S}^{\mathrm{UE,Tx}} & \mathbf{S}^{\mathrm{UE,Rx}} & \mathbf{S}^{\mathrm{UE,UE}}\end{bmatrix}}_{\mathbf{S}} \underbrace{\begin{bmatrix}\mathbf{a}^{\mathrm{Tx}}\\ \mathbf{a}^{\mathrm{Rx}}\\ \mathbf{a}^{\mathrm{UE}}\end{bmatrix}}_{\mathbf{a}}, \tag{2.3}$$

where $\mathbf{S}$ represents the complete scattering matrix describing the reflection, transmission, radiation, and electromagnetic coupling characteristics among the Tx antenna ports, Rx antenna ports, and UE ports. The coupling matrices relevant to the considered IBFD system are defined as follows:

- $\mathbf{S}^{\mathrm{UE,Tx}} \in \mathbb{C}^{K\times N}$ denotes the Tx-to-UE coupling matrix, describing the downlink propagation from the N Tx antenna elements to the K UEs.

- $\mathbf{S}^{\mathrm{Rx,UE}} \in \mathbb{C}^{M\times K}$ denotes the UE-to-Rx coupling matrix, describing the uplink propagation from the K UEs to the M Rx antenna elements.

- $\mathbf{S}^{\mathrm{Rx,Tx}} \in \mathbb{C}^{M\times N}$ represents the Tx-to-Rx coupling matrix, which characterizes the SI channel in the IBFD configuration. This matrix includes all electromagnetic leakage mechanisms between the Tx and Rx arrays, including radiative coupling, conductive coupling, near-field interaction, mutual coupling, and hardware-induced leakage paths.

The desired Tx-to-UE and UE-to-Rx coupling matrices are obtained from the electromagnetic channel formulation described in [56]. In the following analysis, these coupling matrices are treated as the electromagnetic channel representations governing the desired communication paths and the SI coupling mechanism.

Consequently, the overall performance of the IBFD antenna system is determined by the interaction between the desired Tx/UE and UE/Rx channels and the undesired Tx-to-Rx SI coupling. In particular, the Tx excitation matrix affects both the desired radiation toward the UEs and the SI power received by the Rx array. This inherent trade-off motivates the design of transmit and receive beamforming strategies for effective SI suppression while maintaining reliable SU/MU-MIMO IBFD operation.

The base station (BS) transmits the complex baseband symbol vector $\mathbf{s} \in \mathbb{C}^{K\times 1}$ intended for the downlink UEs. The resulting incident power-wave vector at the Tx ports is given by

$$\mathbf{a}^{\mathrm{Tx}} = S_{21}^{\mathrm{PA}}\,\mathbf{W}^{\mathrm{Tx}}\mathbf{s} \quad \in \mathbb{C}^{N\times 1}, \tag{2.4}$$

where S_{21}^{PA} denotes the (assumed identical) forward transmission coefficient of the PAs, which are modeled as linear and narrowband across all Tx chains. The total available power at the Tx array ports is therefore expressed as

$$P_{\mathrm{av}} = \frac{1}{2}\left(\mathbf{a}^{\mathrm{Tx}}\right)^{\mathrm{H}}\mathbf{a}^{\mathrm{Tx}}. \tag{2.5}$$

To simplify the analysis, the receiver front-end is assumed to present a negligible input reflection, such that back-reflections at the LNA inputs can be neglected, i.e., $\mathbf{a}^{\mathrm{Rx}} = \mathbf{0}$. This approximation is reasonable for practical BS receiver designs with high input return loss, which limits reflections from the LNA inputs toward the antenna and RF chains. In addition, the UE terminals are assumed to operate under well-matched IBFD front-ends. Accordingly, and in line with practical full-duplex implementations employing impedance matching networks and circulators to mitigate internal reflections, the self-scattering matrix at the UE ports is approximated as $\mathbf{S}^{\mathrm{UE,UE}} = \mathbf{0}$. Under these assumptions, the outgoing power-wave vector at the UE ports is solely determined by the BS Tx array and is given by

$$\mathbf{b}^{\mathrm{UE}} = \mathbf{S}^{\mathrm{UE,Tx}}\mathbf{a}^{\mathrm{Tx}} \quad \in \mathbb{C}^{K\times 1}. \tag{2.6}$$

In IBFD operation, the Rx array observes a superposition of two contributions: the desired uplink signal and the SI induced by the BS downlink transmission. Therefore, the total outgoing wave vector at the Rx ports is expressed as

$$\mathbf{b}^{\mathrm{Rx}} = \mathbf{b}_{\mathrm{sig}}^{\mathrm{Rx}} + \mathbf{b}_{\mathrm{SI}}^{\mathrm{Rx}} \quad \in \mathbb{C}^{M\times 1}. \tag{2.7}$$

The desired uplink signal component is given by

$$\mathbf{b}_{\mathrm{sig}}^{\mathrm{Rx}} = \mathbf{S}^{\mathrm{Rx,UE}}\mathbf{a}^{\mathrm{UE}}, \tag{2.8}$$

which represents the superposition of signals received from the K user terminals. In parallel, the SI component arises from direct coupling between the Tx and Rx arrays and is given by

$$\mathbf{b}_{\mathrm{SI}}^{\mathrm{Rx}} = \mathbf{S}^{\mathrm{Rx,Tx}}\mathbf{a}^{\mathrm{Tx}}. \tag{2.9}$$

The corresponding coupled power at the Rx array ports is then given by

$$P_{\mathrm{coup}} = \frac{1}{2}\left(\mathbf{b}_{\mathrm{SI}}^{\mathrm{Rx}}\right)^{\mathrm{H}}\mathbf{b}_{\mathrm{SI}}^{\mathrm{Rx}} = \frac{1}{2}\left(\mathbf{a}^{\mathrm{Tx}}\right)^{\mathrm{H}}\left(\mathbf{S}^{\mathrm{Rx,Tx}}\right)^{\mathrm{H}}\mathbf{S}^{\mathrm{Rx,Tx}}\mathbf{a}^{\mathrm{Tx}}. \tag{2.10}$$

Importantly, P_{coup} depends solely on the Tx beamforming matrix $\mathbf{W}^{\mathrm{Tx}}$ and is independent of the Rx beamforming design. Hence, the Tx beamformer directly determines the level of SI entering the Rx front-end and is therefore critical for preventing receiver saturation.

However, P_{coup} characterizes SI only at the antenna/RF port level, prior to spatial combining. After Rx beamforming, the effective SI at baseband depends jointly on the propagation channel and the Rx beamforming matrix. As a result, residual SI can still significantly exceed the desired uplink signal power, necessitating further suppression in the digital and beamforming domains. Accordingly, Rx beamforming is essential to mitigate the residual SI and preserve receiver sensitivity. The total post-LNA SI power and the desired uplink signal power for user k after receive beamforming are defined as

$$P_{\mathrm{SI}} = \frac{1}{2}\left|S_{21}^{\mathrm{LNA}}\right|^2\left\|\left(\mathbf{W}^{\mathrm{Rx}}\right)^{\mathrm{H}}\mathbf{b}_{\mathrm{SI}}^{\mathrm{Rx}}\right\|_2^2, \tag{2.11}$$

$$P_{\mathrm{sig},k} = \frac{1}{2}\left|S_{21}^{\mathrm{LNA}}\right|^2\left|\left(\mathbf{w}_k^{\mathrm{Rx}}\right)^{\mathrm{H}}\mathbf{b}_{\mathrm{sig}}^{\mathrm{Rx}}\right|^2, \tag{2.12}$$

where S_{21}^{LNA} is the forward transmission coefficient of the LNAs, assumed identical, linear, and narrowband across all receive chains.

Radiated Power and Realized Gain

Let $\mathbf{g}_n^{\mathrm{Tx}}(\hat{\mathbf{r}}) = [g_{n,\mathrm{co}}^{\mathrm{Tx}}(\hat{\mathbf{r}}),\, g_{n,\mathrm{xp}}^{\mathrm{Tx}}(\hat{\mathbf{r}})]^{\mathrm{T}}$ denote the EEP of the nth Tx antenna element, representing its complex far-field angular response in the observation direction $\hat{\mathbf{r}}$. The EEP is obtained by exciting the nth Tx port with a unit incident power wave ($a_n^{\mathrm{Tx}} = 1$), while terminating all other antenna ports with matched loads [62]. For the kth downlink beam, the far-field response of the Tx array is determined by the superposition of the individual EEPs weighted by the corresponding beamforming vector. For a UE located in the direction $\hat{\mathbf{r}}_k$, the EEP-based radiation matrix of the Tx array is defined as

$$\mathbf{G}_k^{\mathrm{Tx}} = \left[\mathbf{g}_1^{\mathrm{Tx}}(\hat{\mathbf{r}}_{1,k}),\quad \cdots,\quad \mathbf{g}_N^{\mathrm{Tx}}(\hat{\mathbf{r}}_{N,k})\right] \in \mathbb{C}^{2\times N}. \tag{2.13}$$

The effective isotropic radiated power (EIRP) associated with the kth downlink beam is then given by

$$\mathrm{EIRP}_k\left(\hat{\mathbf{r}}_k\right) = \frac{2\pi}{\eta_0}\left|S_{21}^{\mathrm{PA}}\right|^2\left|\mathbf{G}_{k,\mathrm{co}}^{\mathrm{Tx}}\mathbf{w}_k^{\mathrm{Tx}}\right|^2, \tag{2.14}$$

where η_0 denotes the free-space impedance and $\mathbf{G}_{k,\mathrm{co}}^{\mathrm{Tx}}$ contains the co-polarized components of the EEPs, where co-polarization is defined with respect to Ludwig's third polarization basis [63]. The corresponding field component is taken along the Ludwig-3 co-polar basis vector, rather than a polarization matched to the antenna orientation. To characterize the directional radiation capability of the beamformer independently of the transmit power

level, the transmit realized gain of the kth beam is defined as

$$\mathrm{TxGAIN}_k(\hat{\mathbf{r}}_k) = \frac{4\pi}{\eta_0} \frac{\left|\mathbf{G}_{k,\mathrm{co}}^{\mathrm{Tx}} \mathbf{w}_k^{\mathrm{Tx}}\right|^2}{\|\mathbf{w}_k^{\mathrm{Tx}}\|_2^2}. \tag{2.15}$$

For uplink reception, the corresponding performance metric is the *receive partial realized gain* of the kth uplink beam, which quantifies the effective receiving capability of the Rx beamformer for an incident wave arriving from the direction of UE k. It is defined as

$$\mathrm{RxGAIN}_k\left(\hat{\mathbf{r}}_k\right) = \frac{8\pi\eta_0 P_{\mathrm{sig},k}}{\|E_{k,\mathrm{co}}^{\mathrm{sig}}\|_2^2 \lambda^2}, \tag{2.16}$$

where $E_{k,\mathrm{co}}^{\mathrm{sig}}$ is the co-polarized component of the incident plane wave from uplink user k. While impedance mismatches may reduce the realized gain in practice, this metric remains a useful and physically meaningful measure for evaluating and optimizing Rx beamformer performance under reasonably well-matched conditions.

Isolation Definitions

To characterize the effectiveness of the Tx beamforming strategy in reducing the SI coupled from the Tx array into the Rx array, the **Rx array isolation** is defined as:

$$\mathrm{ISO}^{\mathrm{Rx,Tx}}\left(\mathbf{W}^{\mathrm{Tx}}\right) = \frac{P_{\mathrm{av}}\left(\mathbf{W}^{\mathrm{Tx}}\right)}{P_{\mathrm{coup}}\left(\mathbf{W}^{\mathrm{Tx}}\right)}. \tag{2.17}$$

For an individual Rx element, the coupled SI power at the mth Rx port is expressed as

$$P_{\mathrm{coup},m} = \frac{1}{2}\left(\mathbf{a}^{\mathrm{Tx}}\right)^{\mathrm{H}} \left(\mathbf{S}_m^{\mathrm{Rx,Tx}}\right)^{\mathrm{H}} \mathbf{S}_m^{\mathrm{Rx,Tx}} \mathbf{a}^{\mathrm{Tx}}, \tag{2.18}$$

where $\mathbf{S}_m^{\mathrm{Rx,Tx}} \in \mathbb{C}^{1\times N}$ is the m-th row of the SI coupling matrix $\mathbf{S}^{\mathrm{Rx,Tx}}$. The corresponding isolation metric is referred to as the **Rx element isolation**, denoted by $\mathrm{ISO}_m^{\mathrm{Rx,Tx}}$. In general, the isolation measured at an individual Rx element is higher than the isolation obtained after considering the complete Rx array, as detailed in [53], [54]. Therefore, practical IBFD designs typically select isolation requirements based on the achievable element-level isolation while maintaining sufficient margin to ensure robust operation without unnecessarily restricting the Tx beamforming solution.

After receive beamforming, the residual SI depends on both Tx and Rx beamforming strategies. Therefore, the **total IBFD system isolation** is defined as

$$\mathrm{ISO}^{\mathrm{sys}}\left(\mathbf{W}^{\mathrm{Tx}}, \mathbf{W}^{\mathrm{Rx}}\right) = \frac{P_{\mathrm{av}}\left(\mathbf{W}^{\mathrm{Tx}}\right)}{P_{\mathrm{SI}}\left(\mathbf{W}^{\mathrm{Tx}}, \mathbf{W}^{\mathrm{Rx}}\right)}. \tag{2.19}$$

This metric quantifies the overall SI suppression of the joint Tx/Rx beamforming design.

2.2 Proposed Beamforming Approach

Rx Array Isolation Control

To control SI at the receiver and enable a constrained spatial design, we impose a minimum Tx-to-Rx isolation threshold $\kappa^{\mathrm{Rx,Tx}}$, defined as a design threshold reflecting a receiver-

protection-oriented link-budget constraint:

$$\mathrm{ISO}^{\mathrm{Rx,Tx}}\left(\mathbf{W}^{\mathrm{Tx}}\right) \geq \kappa^{\mathrm{Rx,Tx}}. \tag{2.20}$$

As enforced by (2.20), the achieved Rx array isolation is guaranteed to be greater than or equal to $\kappa^{\mathrm{Rx,Tx}}$, while higher isolation may be obtained depending on the available spatial subspace. Since $\kappa^{\mathrm{Rx,Tx}}$ determines the feasible Tx beamforming subspace, it directly controls the available degrees of freedom (DoF). The feasible subspace for $\mathbf{a}^{\mathrm{Tx}}$ satisfying (2.20) is obtained by solving the (generalized) eigenvalue problem, as derived in [53]:

$$\mathbf{I}_N\, \mathbf{u}_n^{\mathrm{Tx}} = \zeta_n\, (\mathbf{S}^{\mathrm{Rx,Tx}})^{\mathrm{H}} \mathbf{S}^{\mathrm{Rx,Tx}}\, \mathbf{u}_n^{\mathrm{Tx}}, \quad n = 1, \ldots, N, \tag{2.21}$$

where ζ_n represents the isolation metric, ordered as $\zeta_1 \geq \cdots \geq \zeta_N$. Let L denote the number of eigenvalues satisfying $\zeta_n \geq \kappa^{\mathrm{Rx,Tx}}$. The corresponding feasible subspace, common to all Tx beams, is then

$$\{\mathbf{w}_k^{\mathrm{Tx}}\}_{k=1}^{K} \in \mathrm{span}\{\mathbf{u}_1^{\mathrm{Tx}}, \mathbf{u}_2^{\mathrm{Tx}}, \ldots, \mathbf{u}_L^{\mathrm{Tx}}\}. \tag{2.22}$$

Since any linear combination of $\{\mathbf{u}_n^{\mathrm{Tx}}\}_{n=1}^{L}$ will satisfy the isolation constraint, one can also consider Tx beamforming on a beam-to-beam basis, or a linear combination thereof (multi-beam case as discussed above), i.e., for beam k:

$$\mathbf{w}_k^{\mathrm{Tx}} = \mathbf{U}^{\mathrm{Tx}} \boldsymbol{\alpha}_k, \tag{2.23}$$

where $\mathbf{U}^{\mathrm{Tx}} = [\mathbf{u}_1^{\mathrm{Tx}}, \mathbf{u}_2^{\mathrm{Tx}}, \ldots, \mathbf{u}_L^{\mathrm{Tx}}] \in \mathbb{C}^{N \times L}$ and $\boldsymbol{\alpha}_k \in \mathbb{C}^{L \times 1}$ represents the reduced-dimension coefficient vector. Within this subspace, the minimum achievable isolation is $\zeta_L \geq \kappa^{\mathrm{Rx,Tx}}$, which holds for any nonzero $\boldsymbol{\alpha}_k$. For a K-user downlink system employing precoding, a necessary condition for feasibility is that the available Tx subspace provides sufficient spatial DoF, i.e., $L \geq K$. If this condition is not satisfied, exact beamforming becomes infeasible. In such cases, the design must reduce the number of simultaneously served users. This formulation highlights that the Tx beamforming design is fundamentally a spatial DoF-constrained projection problem, in which the effective Tx dimension is reduced from N to L depending on the SI coupling structure and the selected isolation threshold.

SU-MIMO IBFD Architecture: Beamforming Approach

The SU-MIMO case is obtained from the general K-beam IBFD framework when only a single UE is served, i.e., $K = 1$. Consequently, the transmit and receive beamforming matrices reduce to single beamforming vectors, denoted as $\mathbf{w}^{\mathrm{Tx}}$ and $\mathbf{w}^{\mathrm{Rx}}$, respectively.

We propose a joint Tx-Rx beamforming framework [54] that exploits spatial SI suppression at both ends of the link while adapting to the desired beam-steering direction. The Tx beamformer maximizes antenna gain under an SI constraint, while the Rx beamformer extends conventional maximum ratio combining (MRC) with SI suppression.

Tx Beamforming: The Tx beamforming vector is optimized using prior knowledge of the Tx-to-Rx coupling matrix $\mathbf{S}^{\mathrm{Rx,Tx}}$. While the optimization builds upon the structure of a conventional Tx maximum gain beamformer (maxTxGain) [64], it introduces a key modification by enforcing a minimum Rx array isolation threshold, denoted by $\kappa^{\mathrm{Rx,Tx}}$. This threshold is defined based on the ratio between the total available Tx power P_{av} and the LNA 1 dB compression point, while accounting for required backoff due to signal modulation. Enforcing $\kappa^{\mathrm{Rx,Tx}}$ ensures linear operation of the receiver chain by preventing saturation.

The Tx beamforming problem is formulated as follows [53], [54]:

$$\begin{aligned} \max_{\mathbf{w}^{\mathrm{Tx}}} \quad & \mathrm{TxGAIN}(\hat{\mathbf{r}}) \\ \text{subject to} \quad & \begin{cases} \mathrm{ISO}^{\mathrm{Rx,Tx}}\left(\mathbf{w}^{\mathrm{Tx}}\right) \geq \kappa^{\mathrm{Rx,Tx}}, \\ (\mathbf{w}^{\mathrm{Tx}})^{\mathrm{H}}\mathbf{w}^{\mathrm{Tx}} = 1. \end{cases} \end{aligned} \tag{2.24}$$

The optimization is performed within the SI-constrained Tx subspace introduced in the previous section, where the reduced-dimensional excitation vector $\boldsymbol{\alpha}$ is selected to maximize Tx array gain while satisfying the isolation constraint. After obtaining the Tx beamformer $\mathbf{w}_{\mathrm{opt}}^{\mathrm{Tx}}$, the resulting minimum element isolation, $\min(\mathrm{ISO}_m^{\mathrm{Rx,Tx}})$, can be evaluated to verify the receiver protection requirement. If the achieved minimum isolation significantly exceeds the required threshold, $\kappa^{\mathrm{Rx,Tx}}$ can be relaxed to exploit additional spatial DoF and improve Tx gain while maintaining sufficient isolation margin.

Rx Beamforming: Unlike conventional MRC, which only maximizes the desired signal power, the proposed Rx beamformer additionally suppresses residual SI so that the overall IBFD system isolation exceeds κ^{sys}. This threshold is typically selected according to the receiver sensitivity, so that residual SI does not degrade noise-limited performance. The Rx beamforming problem is

$$\begin{aligned} \max_{\mathbf{w}^{\mathrm{Rx}}} \quad & P_{\mathrm{sig}}(\mathbf{w}^{\mathrm{Rx}}) \\ \text{subject to} \quad & \begin{cases} \mathrm{ISO}^{\mathrm{sys}}(\mathbf{w}^{\mathrm{Tx}}, \mathbf{w}^{\mathrm{Rx}}) \geq \kappa^{\mathrm{sys}}, \\ (\mathbf{w}^{\mathrm{Rx}})^{\mathrm{H}}\mathbf{w}^{\mathrm{Rx}} = 1. \end{cases} \end{aligned} \tag{2.25}$$

The optimization problem is solved using the iterative Lagrange multiplier approach proposed in [54]. By jointly optimizing the Tx and Rx beamformers, the SU-MIMO IBFD system achieves effective SI suppression while maintaining high desired signal reception performance, enabling practical full-duplex communication.

MU-MIMO IBFD Architecture: Beamforming Approach

The SU-MIMO formulation is extended to MU-MIMO operation by simultaneously generating $K > 1$ spatial beams. The proposed beamforming framework, introduced in [56], extends the SI-based beamforming design to MU transmission/reception by jointly enforcing SI suppression and multi-user interference (MUI) cancellation.

ZFTx Beamforming: For MU-MIMO downlink transmission, each Tx beam is designed to maximize the received signal at its intended UE while suppressing interference toward the remaining users. Therefore, zero-forcing (ZF) precoding is applied within the SI-constrained transmit subspace. Specifically, the Tx beamforming matrix is restricted to the low-coupling subspace, $\mathbf{U}^{\mathrm{Tx}}$, obtained from the SI isolation formulation as

$$\mathbf{W}^{\mathrm{Tx}} = \mathbf{U}^{\mathrm{Tx}}\mathbf{A}, \tag{2.26}$$

where $\mathbf{A} = \begin{bmatrix} \boldsymbol{\alpha}_1, & \boldsymbol{\alpha}_2, & \cdots, & \boldsymbol{\alpha}_K \end{bmatrix} \in \mathbb{C}^{L \times K}$ is the reduced-dimensional precoding matrix. The ZF condition requires the effective downlink channel $\mathbf{S}^{\mathrm{UE,Tx}}\mathbf{U}^{\mathrm{Tx}}\mathbf{A}$ to have zero off-diagonal elements. The resulting reduced-dimensional ZF solution is

$$\mathbf{A}_{\mathrm{opt}} = \left(\mathbf{U}^{\mathrm{Tx}}\right)^{\mathrm{H}}\left(\mathbf{S}^{\mathrm{UE,Tx}}\right)^{\mathrm{H}}\left[\mathbf{S}^{\mathrm{UE,Tx}}\mathbf{U}^{\mathrm{Tx}}\left(\mathbf{U}^{\mathrm{Tx}}\right)^{\mathrm{H}}\left(\mathbf{S}^{\mathrm{UE,Tx}}\right)^{\mathrm{H}}\right]^{\dagger}. \tag{2.27}$$

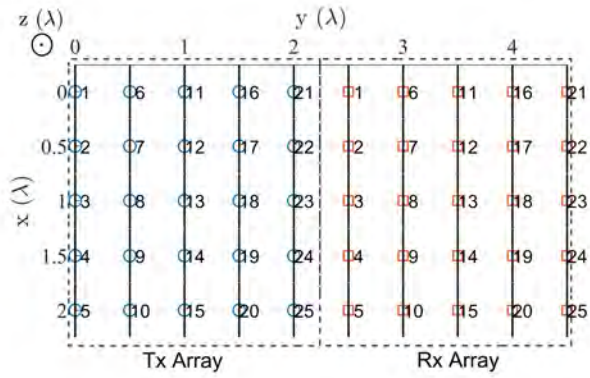


Figure 2.2: Dual-aperture IBFD antenna configuration: 5×5 Tx and Rx arrays of x-polarized dipole antennas, each 0.49λ long with 0.5λ spacing within each array. The operating wavelength $\lambda = \frac{c}{f_c}$, where c is the speed of light and f_c is the design frequency. The arrays are separated by $d = 0.5\lambda$, and both are elevated $\lambda/4$ above a perfect electrically conducting ground plane located in the xy-plane. The H- and E-planes are defined as the yz- and xz-planes, respectively.

where $(\cdot)^{\dagger}$ denotes the Moore–Penrose pseudoinverse. Therefore, the closed-form Tx array beamformer (precoding) matrix with unit-norm column vectors is

$$\mathbf{W}_{\text{opt}}^{\text{Tx}} = \mathbf{U}^{\text{Tx}}\mathbf{A}_{\text{opt}}. \tag{2.28}$$

This formulation satisfies the isolation constraint and suppresses downlink MUI.

ZFRx Beamforming: The Tx beamformer determines the residual SI coupling observed at the receiver. Hence, after Tx-side SI suppression, the remaining SI component is characterized by the residual SI spatial direction $\mathbf{b}_{\text{SI}}^{\text{Rx}}$. The Rx beamformer is then designed to eliminate this residual SI component while suppressing uplink MUI. To enforce SI nulling, the Rx beamforming vectors are constrained to the orthogonal complement of $\mathbf{b}_{\text{SI}}^{\text{Rx}}$. Let $\mathbf{U}^{\text{Rx}} \in \mathbb{C}^{M\times(M-1)}$ denote an orthonormal basis of this null space. Thus, each Rx beamforming vector is parameterized as

$$\mathbf{w}_k^{\text{Rx}} = \mathbf{U}^{\text{Rx}}\boldsymbol{\beta}_k, \tag{2.29}$$

where $\boldsymbol{\beta}_k$ defines the beamforming direction within the SI-free subspace. Collecting the coefficient vectors of all K uplink users gives

$$\mathbf{W}^{\text{Rx}} = \mathbf{U}^{\text{Rx}}\mathbf{B}, \tag{2.30}$$

where $\mathbf{B} \in \mathbb{C}^{(M-1)\times K}$. Consequently, the original MU-MIMO ZF problem is transformed into a reduced-dimensional ZF problem within the SI-null subspace. By forcing the off-diagonal elements of the effective uplink channel to zero, the optimal coefficient matrix is obtained as

$$\mathbf{B}_{\text{opt}} = \left(\mathbf{U}^{\text{Rx}}\right)^{H}\mathbf{S}^{\text{Rx,UE}}\left[\left(\mathbf{S}^{\text{Rx,UE}}\right)^{H}\mathbf{U}^{\text{Rx}}\left(\mathbf{U}^{\text{Rx}}\right)^{H}\mathbf{S}^{\text{Rx,UE}}\right]^{\dagger}. \tag{2.31}$$

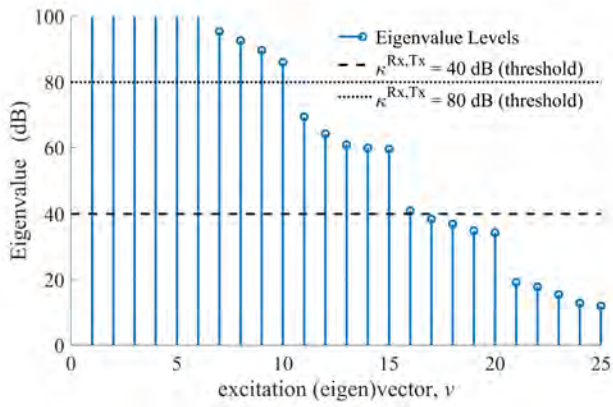


Figure 2.3: Eigenvalue spectrum of $[(\mathbf{S}^{\mathrm{Rx,Tx}})^{\mathrm{H}}\mathbf{S}^{\mathrm{Rx,Tx}}]^{-1}$ for different $\kappa^{\mathrm{Rx,Tx}}$ values.

The final normalized Rx beamforming matrix is

$$\mathbf{W}_{\mathrm{opt}}^{\mathrm{Rx}} = \mathbf{U}^{\mathrm{Rx}}\mathbf{B}_{\mathrm{opt}}, \tag{2.32}$$

which simultaneously eliminates the residual SI component and the uplink MUI under perfect channel knowledge assumptions.

2.3 Proof of Concept: Performance Evaluation

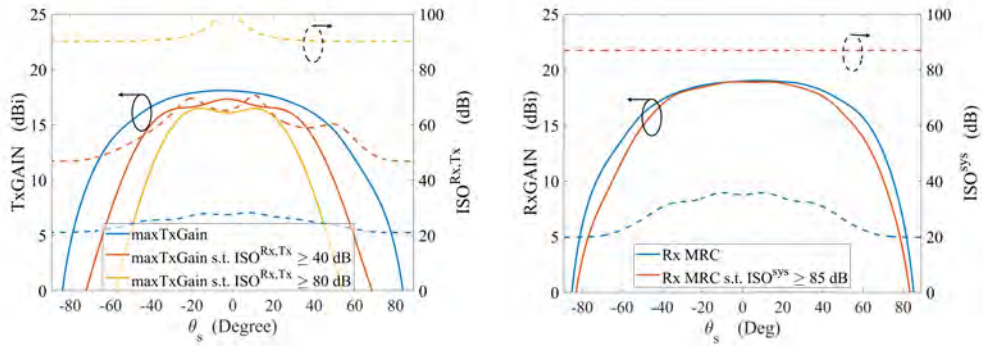
To validate the proposed beamforming framework, a proof-of-concept performance evaluation is conducted using the 5×5 Tx and Rx arrays of x-polarized dipole antennas shown in Figure 2.2. The electromagnetic characteristics of the antenna system are obtained using the in-house Method-of-Moments (MoM) code CAESAR [65], while the beamforming algorithms are implemented and evaluated in MATLAB.

The eigenvalue spectrum of $\left[(\mathbf{S}^{\mathrm{Rx,Tx}})^{\mathrm{H}}\mathbf{S}^{\mathrm{Rx,Tx}}\right]^{-1}$ at f_c, shown in Figure 2.3, directly corresponds to the set of eigenvalues ζ_n defined in (2.21) and characterizes the coupling-dependent spatial DoF used to construct the reduced Tx subspace $\mathbf{U}^{\mathrm{Tx}}$. Larger eigenvalues correspond to weaker coupling modes, whereas smaller values indicate stronger coupling components. Based on this spectrum, eigenmodes are selectively retained according to $\kappa^{\mathrm{Rx,Tx}} = 40$ dB and 80 dB to form the corresponding reduced-dimensional transmission subspaces. These two operating points illustrate the trade-off between SI suppression and the available spatial DoF.

SU-MIMO IBFD Performance

Figure 2.4(a) highlights the trade-off between maximizing the Tx realized antenna gain and enforcing increased isolation levels. As isolation constraints tighten, the realized Tx gain decreases—especially beyond $\pm 40^\circ$ scan angles—demonstrating the cost of aggressive SI suppression. Figure 2.4(b) compares the Rx array gain and IBFD system isolation between a conventional MRC beamformer and the proposed Rx beamformer constrained to $\mathrm{ISO}^{\mathrm{sys}} \geq 85$ dB when the Tx maxGain beamformer is applied to the Tx array. The proposed beamformer maintains comparable gain while significantly enhancing isolation.

Figure 2.5 further illustrates that the proposed Tx beamformer, designed for isolation,



(a) (b)

Figure 2.4: (a) Trade-off between Tx realized array gain and Rx array isolation under varying isolation constraints over H-plane scan angles. (b) Rx array gain and system isolation over H-plane scan angles for MRC vs. proposed Rx beamformer ($\text{ISO}_{\text{sys}} \geq 85$ dB) when maxTxGain beamformer is applied.

produces broader beam patterns in the H-plane due to a reduced set of usable eigenmodes, while maintaining comparable performance in the E-plane. Additionally, while the Tx antenna gain pattern of the proposed beamformer degrades at large H-plane scan angles, its performance in the E-plane remains largely unaffected.

Figure 2.6(a) shows that the achieved element isolation exceeds the array isolation by 10–20 dB, depending on the element index and beamsteering angle. To avoid overdesign, the isolation constraint can be relaxed such that $\min(\text{ISO}_m^{\text{Rx,Tx}})$ more closely approaches the required $\kappa^{\text{Rx,Tx}}$. This is achieved by iteratively adjusting the isolation threshold. For example, as shown in Figure 2.6(b), $\kappa^{\text{Rx,Tx}} = 40$ dB is satisfied after one iteration with $\text{ISO}^{\text{Rx,Tx}} \geq 30$ dB, resulting in $\min(\text{ISO}_m^{\text{Rx,Tx}}) = 57.4$ dB.

To assess the frequency-dependent performance of the center-frequency beamformers, the Tx and Rx coefficients designed at f_c are applied across the 400-MHz operating bandwidth. As shown in Figure 2.7, the center-frequency beamformers maintain their performance over the considered bandwidth. Under the 40-dB Tx isolation constraint, both the minimum Rx-element and Rx-array isolation vary only slightly across the 100-MHz band, whereas the total IBFD system isolation exhibits enhanced suppression within a narrow bandwidth of approximately 2 MHz around f_c. Although this study considers a narrowband proof-of-concept, the proposed framework can be readily extended to wideband operation by constructing independent reduced Tx and Rx subspaces for each subcarrier or subband.

The sensitivity of the proposed approach to practical variations in antenna loading is also investigated. Connecting the beamforming circuitry can perturb the antenna port impedances and consequently affect the Rx array- and element-level isolation. To quantify this effect, the eigenvalue spectrum of the Tx–Rx coupling matrix is evaluated under perturbed loading conditions, where the port impedances are uniformly varied within $Z_0 \pm 0.2Z_0\ \Omega$ to represent potential mismatches introduced by practical beamformer-chip implementations. The resulting variation in Rx array-level isolation remains below 4 dB, while the variation in the minimum Rx element-level isolation remains below 3 dB. These relatively small deviations have a limited impact on the overall system isolation; therefore, the corresponding plots are omitted for brevity.

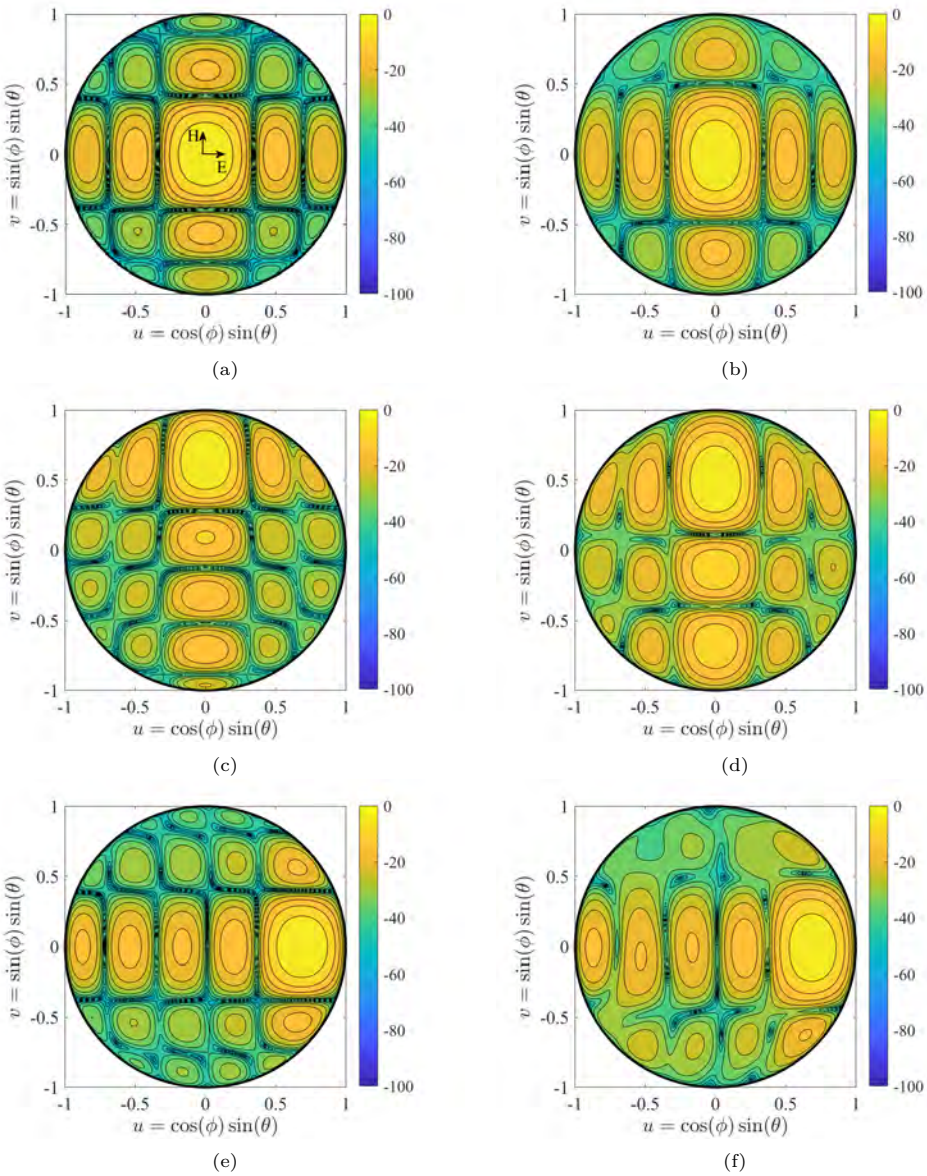
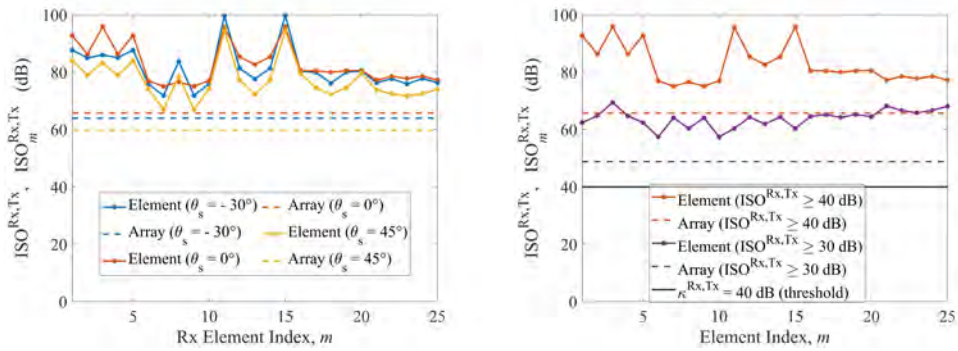


Figure 2.5: Normalized Tx antenna array patterns comparing conventional maxTxGain beamformer vs. proposed beamformer with $\mathrm{ISO}^{\mathrm{Rx,Tx}} \geq 40$ dB: (a)–(b) broadside H-plane; (c)–(d) 45° H-plane; (e)–(f) 45° E-plane.

Overall, the SU-MIMO results demonstrate the trade-off between Tx gain and SI suppression, while showing that the proposed Rx beamformer can substantially improve system isolation with a limited loss in Rx gain. The results also demonstrate that the isolation constraint can be tuned according to the required minimum Rx element-level linearity. The frequency and loading studies further characterize the applicability of the proposed approach under practical operating conditions. These results establish the basis for extending



(a) (b)

Figure 2.6: (a) Rx array vs. element isolation for various H-plane scan angles with $\text{ISO}^{\text{Rx,Tx}} \geq$ 40 dB. (b) Isolation tuning via iterative threshold relaxation for broadside scan.

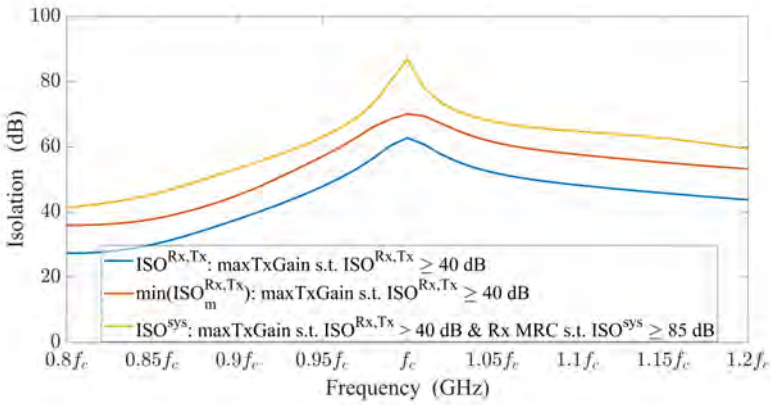


Figure 2.7: Rx minimum-element, array, and total IBFD system isolation at broadside scan over frequency.

the proposed beamforming framework to MU-MIMO IBFD operation.

MU-MIMO IBFD Performance

The proposed beamforming framework is further evaluated in an IBFD MU-MIMO scenario with three simultaneous users, each supporting both uplink and downlink transmission. Figure 2.8(a) compares the Tx EIRP beampatterns obtained with conventional ZFTx and ZFTx constrained by $\text{ISO}^{\text{Rx,Tx}} \geq 40$ dB for steering angles $\theta_k = -25°$, $0°$, and $30°$. Both beamformers preserve the desired main beams and the ZF nulls toward the other users. Introducing the isolation constraint results in only a minor reduction in peak EIRP (less than 1 dB) and a small increase in sidelobe levels. The performance loss depends on the Tx–to–Rx coupling characteristics (e.g., number of antennas and mutual coupling level) and the number of simultaneously supported beams, reflecting the tradeoff between spatial DoF and enforced isolation constraint.

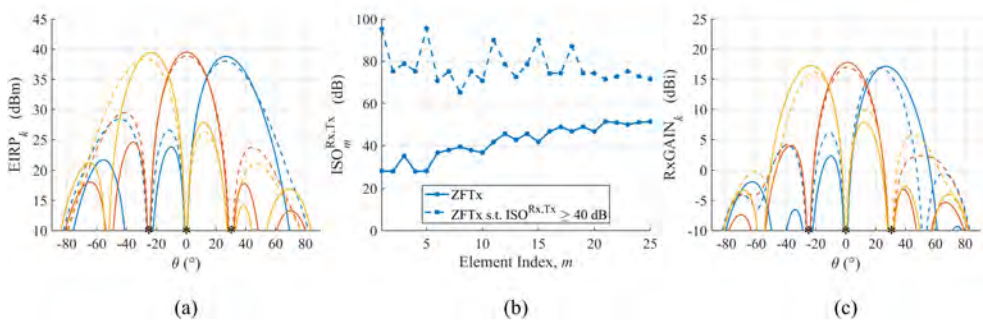


Figure 2.8: (a) Tx EIRP beampatterns at steering angles $\theta_k = -25°, 0°, 30°$ under conventional ZFTx (solid) and ZFTx with $\text{ISO}^{\text{Rx,Tx}} \geq 40$ dB (dashed); (b) Corresponding Rx element isolation obtained from the beamforming weights; (c) Rx array beampatterns for the same steering angles under conventional ZFRx (solid) and SI-Null ZFRx applied with ZFTx design under $\text{ISO}^{\text{Rx,Tx}} \geq 40$ dB (dashed).

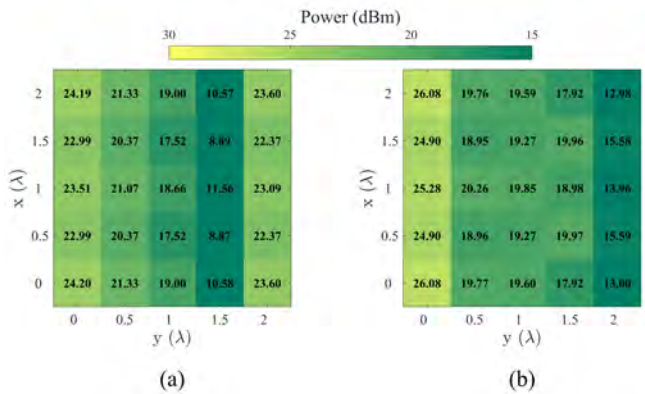


Figure 2.9: Simulated Tx element input power distribution, $\|\mathbf{a}^{\text{Tx}}\|_{\text{dB}}$: (a) conventional ZFTx; (b) ZFTx with $\text{ISO}^{\text{Rx,Tx}} \geq 40$ dB constraint.

The corresponding Rx element isolation is shown in Figure 2.8(b). Conventional ZFTx provides approximately 25–50 dB isolation across the Rx elements, whereas the constrained ZFTx increases the element-level isolation to approximately 65–95 dB, depending on the element location. This improvement results from restricting the Tx excitation to the reduced subspace associated with the weaker Tx–Rx coupling modes.

Figure 2.8(c) shows the Rx beampatterns obtained using conventional ZFRx and the proposed SI-null ZFRx for the constrained Tx beamformer. The desired Rx beams and ZF nulls are preserved, while the SI-null projection provides additional suppression of the residual coupling. The resulting degradation in Rx beamforming performance is small, indicating that the Rx-side null-space projection can effectively complement the Tx-side isolation constraint.

The effect of the isolation constraint on the Tx element excitation is shown in Figure 2.9. The conventional ZFTx solution exhibits a relatively balanced power distribution across the array, with a deviation around column 4. Imposing $\text{ISO}^{\text{Rx,Tx}} \geq 40$ dB produces a similar overall distribution, although a reduction in excitation is observed toward column 5, whose

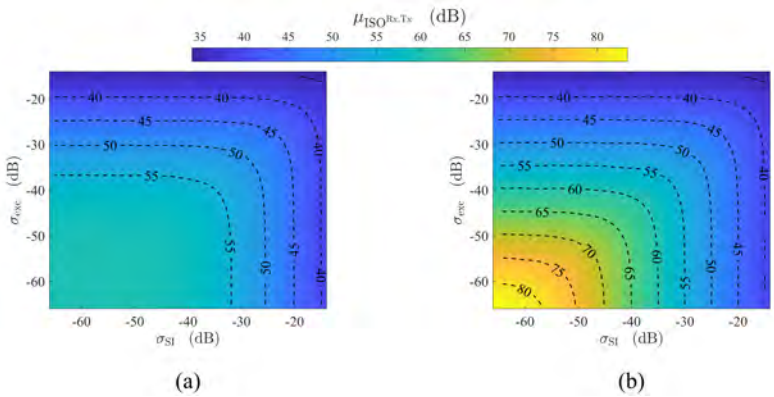


Figure 2.10: Average array isolation, as a function of the standard deviations of Tx excitation and Tx-to-Rx coupling errors. Monte-Carlo results for the ZFTx under: (a) $\mathrm{ISO}^{\mathrm{Rx,Tx}} \geq 40$ dB constraint; (b) $\mathrm{ISO}^{\mathrm{Rx,Tx}} \geq 80$ dB constraint.

elements are closest to the Rx array. This tapering is a direct consequence of restricting the Tx excitation to the reduced SI-avoiding subspace and does not require significant redistribution of power across the remaining elements.

The sensitivity of the ZFTx beamformer is evaluated under perturbations in the Tx excitation vector and Tx–Rx coupling matrix. The perturbed quantities are modeled as

$$\mathbf{a}_{\mathrm{p}}^{\mathrm{Tx}} = \mathbf{a}^{\mathrm{Tx}} + \boldsymbol{\delta}_{\mathrm{exc}}, \qquad \mathbf{S}_{\mathrm{p}}^{\mathrm{Rx,Tx}} = \mathbf{S}^{\mathrm{Rx,Tx}} + \boldsymbol{\Delta}_{\mathrm{SI}}, \tag{2.33}$$

where $\boldsymbol{\delta}_{\mathrm{exc}} \in \mathbb{C}^{N\times 1}$ and $\boldsymbol{\Delta}_{\mathrm{SI}} \in \mathbb{C}^{M\times N}$ represent excitation and coupling perturbations, respectively, with entries modeled as independent complex Gaussian random variables, $\delta_{\mathrm{exc},n} \sim \mathcal{CN}(0, \sigma_{\mathrm{exc}}^2)$ and $\Delta_{\mathrm{SI},mn} \sim \mathcal{CN}(0, \sigma_{\mathrm{SI}}^2)$. The resulting array isolation is evaluated according to (2.17). Excitation errors primarily perturb the beamforming solution, whereas coupling errors directly modify the SI channel and therefore the achievable suppression.

Figure 2.10 summarizes a 1500-trial Monte-Carlo analysis. Increasing either σ_{exc} or σ_{SI} reduces the average array isolation, with a substantially higher sensitivity observed for the stringent $\mathrm{ISO}^{\mathrm{Rx,Tx}} \geq 80$ dB constraint. In this case, maintaining the target isolation requires approximately $\sigma_{\mathrm{exc}} < -60$ dB and $\sigma_{\mathrm{SI}} < -55$ dB (see Figure 2.10(b)). Notably, the element isolation levels remain consistently higher than the corresponding array-level isolation, since the coherent combination of coupling contributions across all Rx elements determines it.

Overall, the MU-MIMO results demonstrate that the proposed Tx–Rx beamforming framework suppresses SI while preserving the DoF required for MU-ZF. A 40 dB Tx–Rx isolation constraint causes only a minor degradation in the desired Tx and Rx beam patterns and requires no substantial change in the Tx power distribution. The sensitivity analysis further shows that moderate implementation errors have limited impact, while more stringent isolation targets result in greater sensitivity to excitation and coupling uncertainties.

CHAPTER 3

Integrated IBFD Testbed: Design and Experimental Validation

This chapter presents the experimental implementation and validation of the proposed integrated in-band full-duplex (IBFD) beamforming framework. A practical IBFD testbed is developed by integrating separate-aperture transmit (Tx) and receive (Rx) Vivaldi antenna arrays with a Zynq UltraScale+ RFSoC platform. The resulting platform enables coherent signal generation, acquisition, digital beamforming, and measurement of the Tx–Rx coupling that governs self-interference (SI) in the system.

The experimental study is organized in three stages. First, the antenna arrays, RFSoC platform, and measurement methodology are described. The relevant hardware nonidealities are also characterized to establish the practical limitations of the measurement system. Second, the proposed beamforming framework is experimentally validated for single-user multiple-input multiple-output (SU-MIMO) and multi-user multiple-input multiple-output (MU-MIMO) IBFD operation. These experiments demonstrate the ability of the proposed Tx–Rx beamforming strategy to suppress SI while preserving the desired spatial transmission and reception characteristics. Finally, the same physical platform is extended to a full-duplex (FD) radar application. The radar experiment investigates whether the SI-based Tx beamforming strategy can suppress the direct Tx–Rx coupling sufficiently to recover target echoes in a frequency-modulated continuous-wave (FMCW) radar measurement.

3.1 Integrated IBFD Testbed and Measurement Methodology

To experimentally validate the proposed beamforming framework, a practical IBFD testbed was developed. The selected case study, illustrated in Figure 3.1, comprises separate-aperture side-by-side 3×5 Tx and Rx Vivaldi antenna arrays operating over the 3–6 GHz frequency range [57]. The arrays are fabricated using 3D printing and silver coating and are positioned with an electrically small separation of 0.5λ at 6 GHz, resulting in strong mutual coupling between the Tx and Rx arrays while avoiding grating lobes during beam steering across the operating frequency range. This configuration provides a challenging and representative scenario for evaluating the effectiveness of the SI mitigation approach.

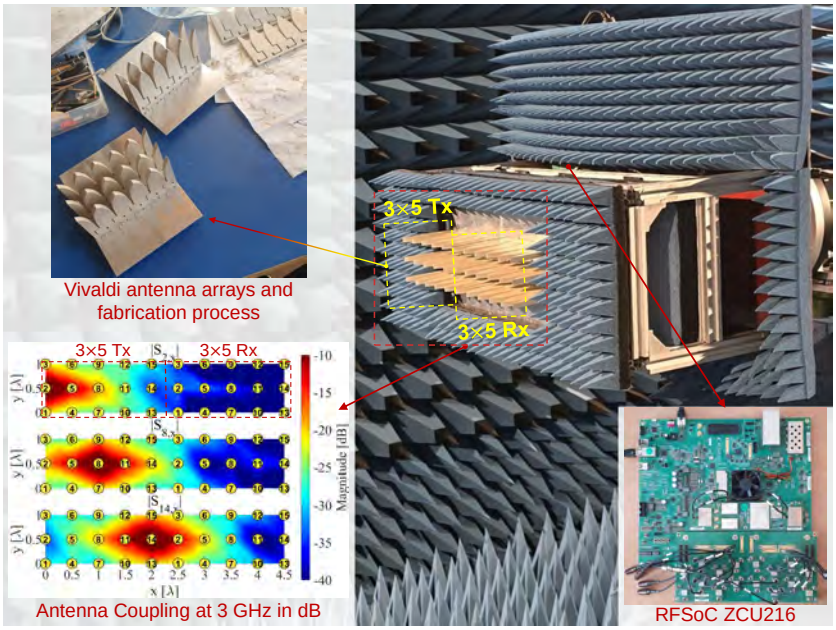


Figure 3.1: Case study: Experimental IBFD antenna system comprising side-by-side 3×5 Tx and Rx Vivaldi antenna arrays fabricated using 3D printing and silver coating. The system is integrated with the Zynq UltraScale+ RFSoC ZCU216 evaluation kit and deployed inside an anechoic chamber for measurement and validation. **Left-top inset**: Photograph of the Vivaldi antenna array and its manufacturing process. **Left-bottom inset**: Simulated antenna-only coupling at 3 GHz from representative left-edge, center, and right-edge Tx elements to all Rx elements. **Right-bottom inset**: Photograph of the ZCU216 evaluation board. (adapted from [54], [56])

Tx–Rx Antenna Array Design

Antenna Element Structure: Each antenna element is based on a Vivaldi design, realized from a single 3D-printed and subsequently metalized structure. The feed is implemented via a $50\,\Omega$ coaxial probe connected through the ground plane. Figure 3.2(a) shows the unit-cell model of the proposed Vivaldi element, highlighting the optimized parameters, including cavity size, slot geometry, Vivaldi taper length, and taper opening rate [66].

Manufacturing Process: A small-scale 1×5 array prototype was first fabricated using a Halot Mage 8K Resin 3D printer, offering a fine $29.7\,\mu$m XY resolution and compatibility with light-reactive thermoset materials. Post-printing, the antenna structures were cleaned and subsequently coated with multiple layers of water-based silver conductive paint (842WB) using a manual brush application. This process resulted in electrically conductive and mechanically stable antenna surfaces. Figure 3.2(b) presents the final silver-coated 1×5 Vivaldi array with integrated coaxial probe feeds.

Simulation and Experimental Validation: Simulations of the infinite array model showed active reflection coefficients less than -10 dB for beam steering up to $\pm 60^\circ$ in the E-plane and $\pm 50^\circ$ in the H-plane across the 3–6 GHz band. Measurements on the fabricated 1×5 array prototype confirmed these simulation results, validating the embedded element design and coaxial feed structure, as detailed in [57].

Full Tx–Rx Array Implementation: Building on the validated antenna design, the

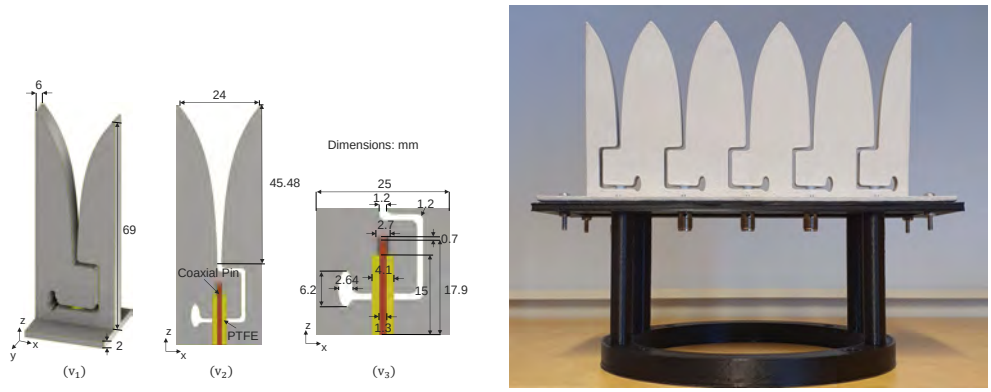


Figure 3.2: Vivaldi antenna array development: (a) Unit-cell geometry; (v_1) 3D view of the model, (v_2) Cross-section of the antenna element in the x-z plane, and (v_3) Detailed view of the feeding section (see the original in Fig. 1 in [57]), (b) 3D-printed and silver-coated 1×5 Vivaldi array prototype.

configuration was extended to the full 3×5 Tx and Rx arrays used in the IBFD testbed. Each array is implemented on a separate aluminum ground plane, with an individual coaxial probe feed provided for each antenna element, as illustrated in Figure 3.1.

The RFSoC ZCU216 Platform

The antenna arrays are interfaced with a Zynq UltraScale+ RFSoC ZCU216 evaluation platform through a custom-designed printed circuit board incorporating commercial off-the-shelf baluns[1]. The baluns convert the differential DAC outputs to single-ended signals for transmission and convert the single-ended received signals to differential signals for the ADC inputs. The RFSoC's internal data converters are used directly, without external power amplifiers (PAs) or low-noise amplifiers (LNAs).

The ZCU216 integrates the RF data converters and programmable processing resources required for signal generation, acquisition, and digital beamforming. Its high level of integration enables the proposed beamforming and SI cancellation algorithms to be evaluated using the same hardware platform that generates and acquires the RF signals. The platform also provides the timing and processing resources required for system calibration and experimental control [29], [67].

The board contains 16 DACs and 16 ADCs, each with 14-bit resolution, organized into four DAC tiles and four ADC tiles. The RF interfaces support direct RF conversion over the operating frequency range. The DACs provide sampling rates of up to 10 GSPS, while the ADCs support sampling rates of up to 2.5 GSPS. These capabilities enable direct generation and acquisition of the RF signals without additional analog frequency-conversion stages.

Clock Synchronization: Precise synchronization between the transmit and receive paths is critical for coherent digital beamforming and effective SI cancellation. However, the independent phase-locked loops (PLLs) associated with the DAC and ADC tiles can introduce phase offsets and clock misalignment, which may degrade coherent operation and consequently affect beamforming and cancellation performance. To address this issue, the

[1] Product No.: X4BD40L1-50100G

RFSoC architecture provides a multi-tile synchronization (MTS) feature. MTS uses a shared reference clock and a system reference (SYSREF) signal to synchronize the sample clocks across the DAC and ADC tiles [68]. When properly configured, MTS provides deterministic phase alignment and consistent timing across the RF interfaces.

In practice, however, achieving reliable MTS on the ZCU216 with the default clock configuration can be challenging. In particular, mismatched PLL divider settings and improper SYSREF routing can result in synchronization errors and phase misalignment across channels. Therefore, the PLL configuration and SYSREF routing must be carefully tuned to establish coherent operation across the RF interfaces [58]. Establishing this coherent operating condition is an essential step because the proposed beamforming framework relies on accurate relative amplitude and phase control across the array elements.

IBFD Measurement Architecture

The integrated antenna–RFSoC measurement platform is illustrated in Figure 3.3. The RFSoC generates and acquires the signals required for the Tx and Rx arrays, while a movable probe antenna is used for Tx and Rx embedded element patterns (EEPs) characterization. The probe can be switched between two amplifiers, Amp1 and Amp2, each providing 50 dB gain to compensate for free-space propagation losses during measurements. Amp1 is typically used for reception and Amp2 for transmission, depending on the measurement step.

The measurement process begins with the generation of a discrete-time signal representing a continuous-wave tone at the carrier frequency ω_c. Although the standard Xilinx graphical user interface provides basic waveform-generation capabilities, an in-house MATLAB function is used to generate the time-domain samples with improved spectral purity and reduced spurious content [58]. The generated signal is expressed as

$$g[n] = \mathfrak{Re}\{U_{\mathrm{t}} e^{jn\omega_c/f_{\mathrm{s}}}\}, \tag{3.1}$$

where $n \in \mathbb{Z}$ is the discrete time index, f_{s} is the DAC sampling frequency, and U_{t} is a complex phasor representing the signal amplitude and phase.

The complex phasor U_{t} is weighted by the Tx beamforming vector $\mathbf{w}^{\mathrm{Tx}}$ to form the 15×1 vector $\mathbf{U}_{\mathrm{t}}$. The corresponding synchronized analog signals, denoted by $\mathbf{a}^{\mathrm{Tx}} \propto \mathbf{U}_{\mathrm{t}}$, are generated by the DACs, converted to single-ended signals through the baluns, and incident onto the Tx antenna array.

At the receive side, the signals collected by the Rx array are converted to differential signals through the corresponding baluns and digitized by the ADCs. The received signals are represented by two 15×1 vectors, $\mathbf{b}_{\mathrm{sig}}^{\mathrm{Rx}}$ and $\mathbf{b}_{\mathrm{SI}}^{\mathrm{Rx}}$, corresponding to the desired signal and SI components, respectively. After digitization, the resulting digital signals, $\mathbf{U}_{\mathrm{sig}} \propto \mathbf{b}_{\mathrm{sig}}^{\mathrm{Rx}}$ and $\mathbf{U}_{\mathrm{SI}} \propto \mathbf{b}_{\mathrm{SI}}^{\mathrm{Rx}}$, are combined using the conjugate-transposed Rx beamforming vector $(\mathbf{w}^{\mathrm{Rx}})^{\mathrm{H}}$ to obtain the corresponding scalar outputs U_{sig} and U_{SI}.

All signal generation, RFSoC control, data acquisition, and subsequent processing are implemented through MATLAB. The acquired time-domain samples are analyzed in the frequency domain using the Fast Fourier Transform (FFT).

The complete measurement procedure consists of the following steps:

- **Tx EEP Measurements:** The probe antenna is connected to Amp2 through switch position 2. Each Tx array element is excited individually with a 1 V signal while the remaining elements are terminated. The voltage measured at the probe, $U_{\mathrm{r}}^{\mathrm{probe}}$, is recorded and used to characterize the corresponding Tx EEP.

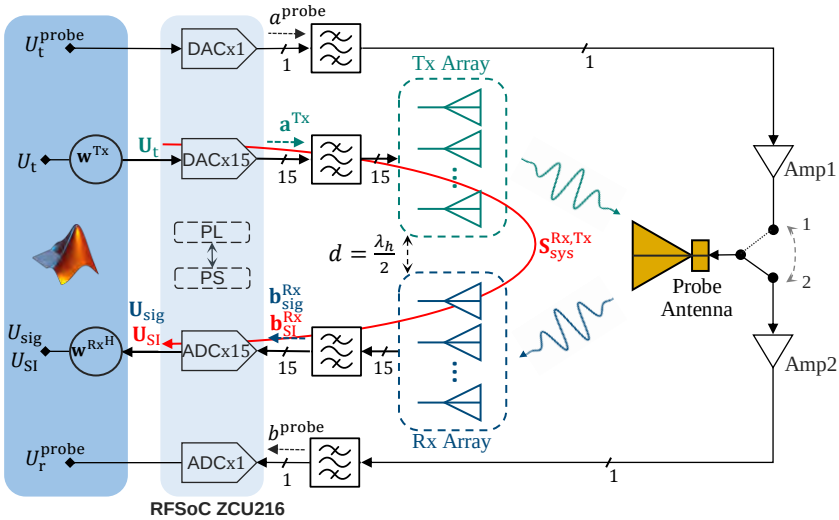


Figure 3.3: Block diagram of the integrated IBFD antenna–RFSoC measurement platform. The DACs generate the transmit signals for the Tx array, while the ADCs capture the received signals at the Rx array. A movable probe antenna connected to either Amp1 or Amp2 is used for antenna-element characterization and coupling-matrix measurements.

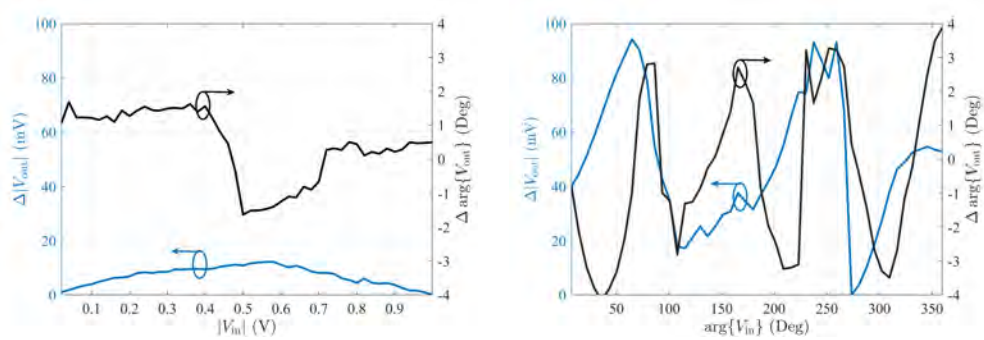
- **Rx EEP Measurements:** The probe antenna is switched to the receive configuration through position 1 and used as the transmitting antenna with $U_t^{probe} = 1$ V. The voltages measured at the individual Rx array elements are recorded to characterize their corresponding Rx EEPs.

- **Coupling Matrix Measurement:** With the probe antenna turned off, each Tx array element is sequentially excited with a 1 V signal while all other Tx elements are terminated. The resulting voltages measured at the Rx elements form the columns of the system coupling matrix $\mathbf{S}_{sys}^{Rx,Tx}$, which relates the Tx excitation vector to the received SI according to

$$\mathbf{U}_{SI} = \mathbf{S}_{sys}^{Rx,Tx}\mathbf{U}_t. \tag{3.2}$$

- **Beamformer Optimization:** The measured Tx EEPs and system coupling matrix $\mathbf{S}_{sys}^{Rx,Tx}$ are used to determine the Tx beamformer according to the optimization criterion in (2.24) and (2.28). For this optimization, $\mathbf{S}^{Rx,Tx}$ is represented by the measured system coupling matrix, i.e., $\mathbf{S}^{Rx,Tx} = \mathbf{S}_{sys}^{Rx,Tx}$, and the Tx incident power wave vector is represented by $\mathbf{a}^{Tx} = \mathbf{U}_t$, since the proportionality factors cancel when evaluating the relevant power ratios. Subsequently, the Rx beamformer is optimized according to (2.25) and (2.32) to achieve the target residual SI suppression level.

DAC/ADC Nonlinearity Characterization: Before evaluating the IBFD beamforming performance, the nonlinear behavior of the RFSoC DAC/ADC signal chain is characterized using a DAC-to-ADC loopback configuration. This test is performed to quantify amplitude and phase errors introduced by the hardware and to distinguish these effects from those associated with the beamforming measurements. The input DAC signal is characterized by its amplitude, $|V_{in}|$, and phase, $\arg\{V_{in}\}$, while the corresponding amplitude, $\Delta|V_{out}|$, and phase, $\Delta\arg\{V_{out}\}$, deviations at the ADC output.



(a) (b)

Figure 3.4: $\Delta|V_{\text{out}}|$ and $\Delta \arg\{V_{\text{out}}\}$ at the ADC output for DAC-to-ADC loopback structure: (a) varying $|V_{\text{in}}|$ for fixed $\arg\{V_{\text{in}}\}$; (b) varying $\arg\{V_{\text{in}}\}$ for fixed $|V_{\text{in}}|$.

Figure 3.4(a) shows the measured response as the input amplitude $|V_{\text{in}}|$ is varied while $\arg\{V_{\text{in}}\}$ is fixed. The amplitude error, $\Delta|V_{\text{out}}|$, exhibits a relatively small nonlinear variation over the tested amplitude range, while the phase error varies approximately between -1.5° and 1.5°. When the input phase $\arg\{V_{\text{in}}\}$ is varied at a fixed amplitude, as shown in Figure 3.4(b), the amplitude error exhibits a stronger variation, reaching approximately 80 mV, while the phase error varies between approximately -4° and 4°. The sharp transitions observed in the phase-dependent response indicate increased sensitivity of the DAC/ADC chain to the input phase.

Overall, the loopback measurements show that the RFSoC signal chain introduces amplitude- and phase-dependent errors. These effects establish the hardware-related error floor to consider when interpreting the subsequent antenna and beamforming measurements.

3.2 IBFD Validation Results and Discussion

The experimental results presented in this section validate the proposed joint Tx–Rx beamforming framework using the integrated IBFD testbed. The validation is divided into SU-MIMO and MU-MIMO configurations. The SU-MIMO experiment first establishes the SI suppression and beamforming trade-off for a single spatial stream. The MU-MIMO experiment then extends the evaluation to multiple simultaneously generated beams.

SU-MIMO IBFD Validation

The SU-MIMO configuration provides the initial experimental validation of the proposed beamforming framework. A single spatial beam ($K = 1$) is generated using the Tx and Rx antenna arrays, and the measured Tx–Rx coupling matrix is characterized at $f_c = 3.5$ GHz.

The eigenvalue spectrum, computed from both simulated and measured Tx-to-Rx coupling matrices, provides insight into the available DoF for optimizing the Tx beamformer. Figure 3.5 shows the eigenvalue spectrum of the matrix $\left[(\mathbf{S}^{\text{Rx,Tx}})^{\text{H}}\mathbf{S}^{\text{Rx,Tx}}\right]^{-1}$. The number of dominant eigenvalues above the threshold $\kappa^{\text{Rx,Tx}} = 45$ dB determines the effective number of available DoF for beamforming optimization[2]. The dominant coupling modes (small eigenvalues) show good agreement between simulation and measurement, whereas

[2] A threshold of $\kappa^{\text{Tx,Rx}} = 45$ dB corresponds to a maximum available transmit power $P_{\text{av}} \approx 12$ dBm, assuming the LNA 1-dB compression point with modulation-induced backoff is approximately -33 dBm.

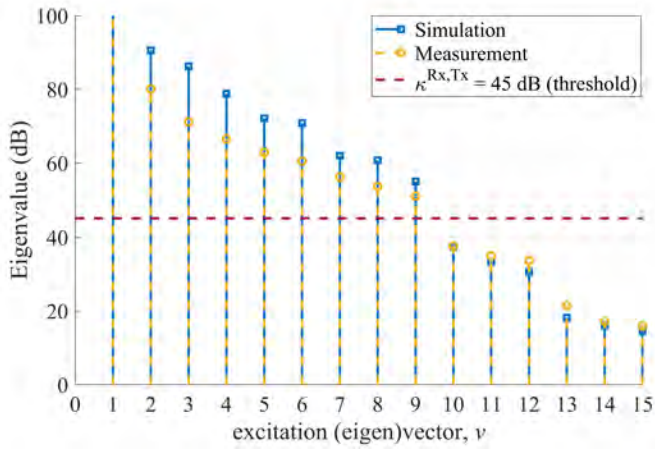


Figure 3.5: Eigenvalue spectrum of $[(\mathbf{S}^{\mathrm{Rx,Tx}})^{\mathrm{H}}\mathbf{S}^{\mathrm{Rx,Tx}}]^{-1}$ at $f_c = 3.5$ GHz.

deviations in the weaker modes (high eigenvalues) are attributed primarily to the finite receiver dynamic range ($\approx$ 80–84 dB) and residual calibration and phase errors ($\pm 4^\circ$), to which weak eigenmodes are particularly sensitive.

The impact of the Tx beamformer on the Rx-side isolation is first evaluated using the conventional maxTxgain beamformer as a reference. Figure 3.6(a) shows the resulting Rx minimum element and array isolation over the E-plane scan angles. The conventional beamformer provides isolation levels between approximately 17 and 27 dB. In contrast, the proposed Tx beamformer exploits the available DoF identified from the eigenvalue analysis to impose the coupling constraint during beamformer optimization. As shown in Figure 3.6(b), the resulting Rx isolation exceeds 45 dB over the considered scan range.

The simulation and measurement results exhibit good agreement at moderate isolation levels, while larger discrepancies become apparent as the target isolation increases. To investigate the sensitivity of the proposed beamformer to practical hardware impairments, an additional $\pm 4^\circ$ random phase error was introduced into the Tx incident power waves $\mathbf{a}^{\mathrm{Tx}}$ in the simulations. The resulting degradation is relatively small at moderate isolation levels but becomes more noticeable as the isolation target increases. This behavior is consistent with the increased sensitivity of deep-suppression conditions to phase errors and the amplitude- and phase-dependent errors identified in the DAC/ADC loopback characterization. Nevertheless, the measured results remain consistent with the expected performance of the proposed beamforming approach.

The Rx beamforming stage is subsequently applied to suppress the residual SI after Tx-side isolation. A system isolation target of $\kappa^{\mathrm{sys}} = 80$ dB is selected because the preceding analysis shows that this level introduces little or no penalty in beamforming gain. Figure 3.6(b) shows that the proposed joint Tx–Rx beamformer consistently achieves total system isolation exceeding 80 dB over the considered scan range. The remaining differences between simulation and measurement are attributed to RFSoC amplitude and phase errors, converter nonlinearity, calibration imperfections, and finite system dynamic range.

Having established the SI mitigation performance, the corresponding impact on the desired-signal beamforming gain is evaluated next. Figure 3.7(a) shows the normalized maximum Tx and Rx beamforming gains over the E-plane scan angles. The measured and

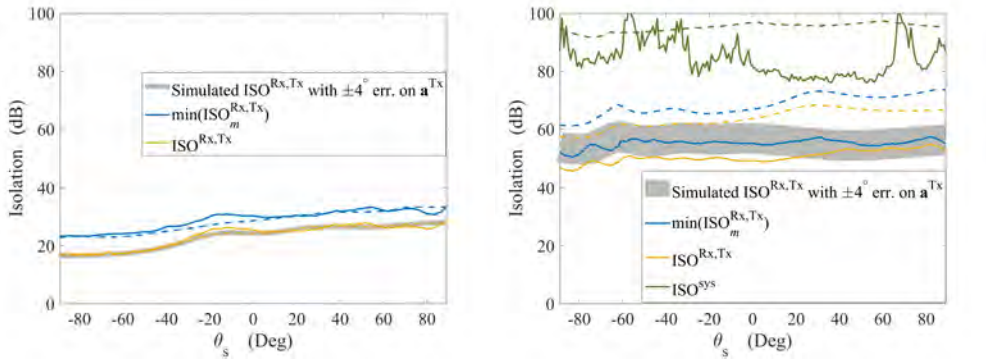


Figure 3.6: Simulation (dashed) and measurement (solid) comparison of isolation over E-plane scan angles: (a) Rx minimum-element and array isolation using the conventional Tx maximum-gain beamformer; (b) Rx minimum-element, array, and total system isolation using the proposed Tx beamformer with $\kappa^{\mathrm{Rx,Tx}} = 45$ dB and subsequent Rx beamforming with $\kappa^{\mathrm{sys}} = 80$ dB.

simulated results generally follow the same trend. A discrepancy is observed in the Tx gain at positive scan angles, which is primarily attributed to radiation from the ground-plane edge absorbers in the measurement setup, an effect not included in the simulation model. At large negative scan angles, the proposed Tx beamformer also exhibits a reduction in gain relative to the conventional maximum-gain beamformer, reaching approximately 4.5 dB at $-30°$. This reduction results from restricting the Tx excitation to the subset of beamforming vectors satisfying the $\kappa^{\mathrm{Rx,Tx}}$ isolation constraint. The Rx gain follows the simulated response over most scan angles, with larger discrepancies at extreme angles due to the measurement environment and increased residual interference, as illustrated in Figure 3.7(a).

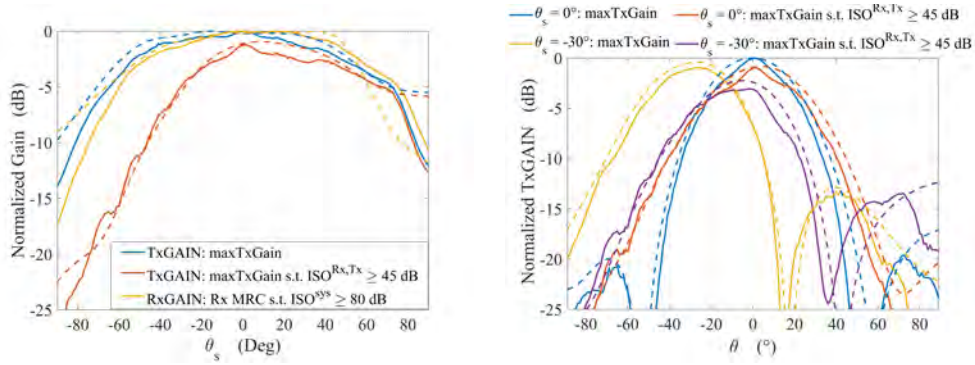
To further evaluate the effect of the isolation constraint on the Tx radiation characteristics, the Tx array beam patterns were measured and simulated over E-plane angles from $-90°$ to $90°$. Figure 3.7(b) shows the normalized Tx array radiation patterns for a representative scan angle of $-30°$ and at broadside. The proposed beamforming method produces a wider radiation pattern than the conventional maxTxgain beamformer, reflecting the inherent trade-off between beam directivity and the stringent Tx–Rx isolation constraint.

Overall, the SU-MIMO measurements demonstrate that the proposed joint Tx–Rx beamforming strategy can provide substantial SI suppression while maintaining the desired spatial beamforming characteristics.

MU-MIMO IBFD Validation

The MU-MIMO experiment extends the validation to multiple simultaneous spatial streams. Two beams are generated concurrently by the Tx and Rx arrays, and the measured Tx–Rx coupling matrix is used for the subsequent zero-forcing Tx (ZFTx) and zero-forcing Rx (ZFRx) beamformer optimization. The experiments are performed at $f_c = 3$ GHz.

The coupling eigenvalue spectrum at this frequency is shown in Figure 3.8. The measured spectrum follows the simulated result over the dominant coupling modes, confirming that the experimentally characterized coupling matrix provides a suitable basis for multi-beam beamformer optimization. This spectrum is also measured later in the FD-radar experiment.



(a) (b)

Figure 3.7: Simulation (dashed) and measurement (solid) comparison of beamforming performance over E-plane scan angles: (a) maximum Tx and Rx beamforming gains obtained with the proposed joint Tx–Rx beamformer using $\kappa^{\mathrm{Rx,Tx}} = 45$ dB and $\kappa^{\mathrm{sys}} = 80$ dB; (b) normalized Tx array radiation patterns at selected E-plane scan angles for the conventional maxTxgain and proposed Tx beamformers.

The first MU-MIMO beamforming case is shown in Figure 3.9, where two beams are simultaneously steered toward $\theta_k = -10^\circ$ and $\theta_k = 20^\circ$. Figures 3.9(a) and (c) show the normalized Tx and Rx gain patterns, respectively, obtained using the conventional and proposed ZF beamformers. The proposed ZFTx beamformer preserves the desired main-lobe directions and ZF characteristics while introducing a modest reduction in peak Tx gain and a slight increase in sidelobe levels. Similarly, the proposed ZFRx beamformer maintains the desired receive directions with only a small degradation in peak gain. The good agreement between simulation and measurement confirms that the proposed beamformers preserve the desired spatial selectivity under the imposed SI constraints.

The corresponding Rx element isolation is shown in Figure 3.9(b). As in the SU-MIMO case, the isolation constraint is imposed at the Rx-array level, i.e., on the total received SI power across all Rx elements rather than independently on each element. Enforcing $\mathrm{ISO}^{\mathrm{Rx,Tx}} \geq 45$ dB results in substantially higher per-element isolation, with values reaching approximately 60–80 dB depending on the beam directions. Compared with the unconstrained Tx beamformer, improvements of up to approximately 50 dB are obtained.

The second MU-MIMO beamforming case, shown in Figure 3.10, considers beams steered toward $\theta_k = 0^\circ$ and $\theta_k = 30^\circ$. The proposed ZFTx beamformer again maintains the desired Tx beam directions while satisfying the coupling constraint. The corresponding ZFRx beamformer preserves the receive beam directions with limited gain degradation.

The consistency between the two MU-MIMO configurations demonstrates that the proposed framework is not restricted to a particular beam arrangement. Instead, the available spatial DoF can be exploited to simultaneously form multiple desired beams and suppress the strong Tx–Rx coupling. This provides the experimental basis for extending the same SI-based spatial beamforming principle to other full-duplex applications, including the radar experiment considered next.

3.3 Full-Duplex Radar Validation Results

The preceding sections established the physical IBFD platform and experimentally validated the proposed beamforming framework for SU- and MU-MIMO communication scenarios.

The final experiment extends the same platform to full-duplex (FD) radar and investigates whether the available low-coupling spatial DoF can be exploited to improve target detection. The radar-specific formulation and experimental study are reported in [59]. In the present section, the emphasis is on how this radar application is realized using the experimentally validated IBFD platform and on the resulting SI suppression and target-detection.

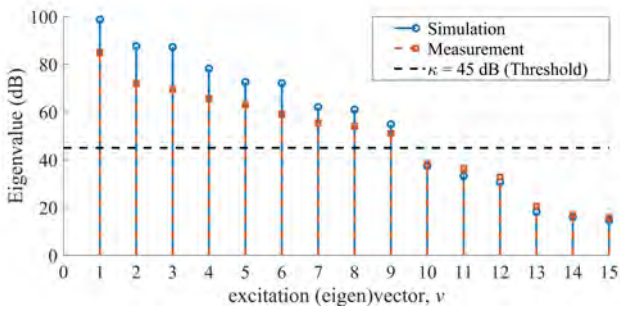
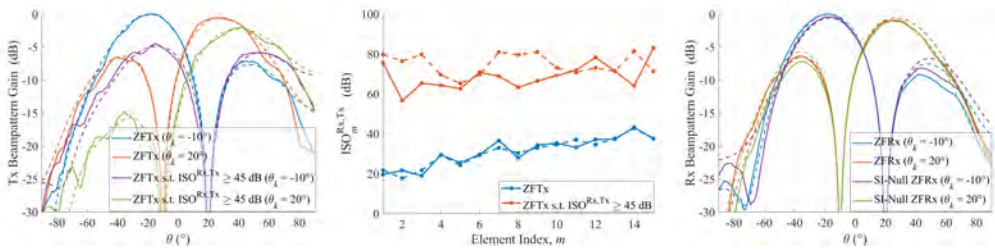
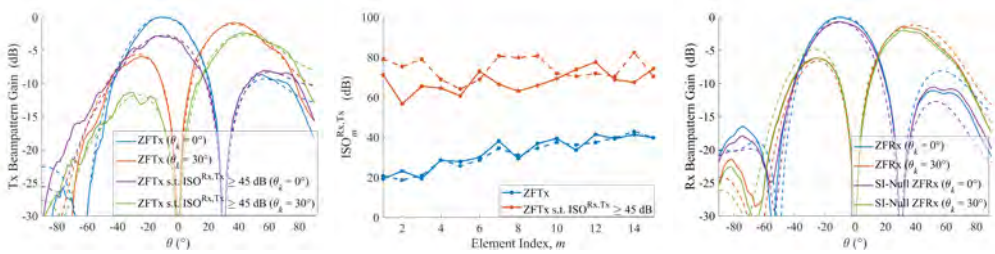


Figure 3.8: Eigenvalue spectrum of $[(\mathbf{S}^{\mathrm{Rx,Tx}})^{\mathrm{H}}\mathbf{S}^{\mathrm{Rx,Tx}}]^{-1}$ at $f_c = 3$ GHz.



(a) (b) (c)

Figure 3.9: Simulation (dashed) and measurement (solid) results for the first MU-MIMO beamforming case, with beams steered toward $\theta_k = -10°$ and $\theta_s = 20°$: (a) normalized Tx gain patterns for the conventional maxTxGain and proposed ZFTx beamformers; (b) corresponding Rx element isolation; (c) normalized Rx gain patterns for the conventional and proposed ZFRx beamformers.



(a) (b) (c)

Figure 3.10: Simulation (dashed) and measurement (solid) results for the second MU-MIMO beamforming case, with beams steered toward $\theta_k = 0°$ and $\theta_s = 30°$: (a) normalized Tx gain patterns; (b) corresponding Rx element isolation; (c) normalized Rx gain patterns.

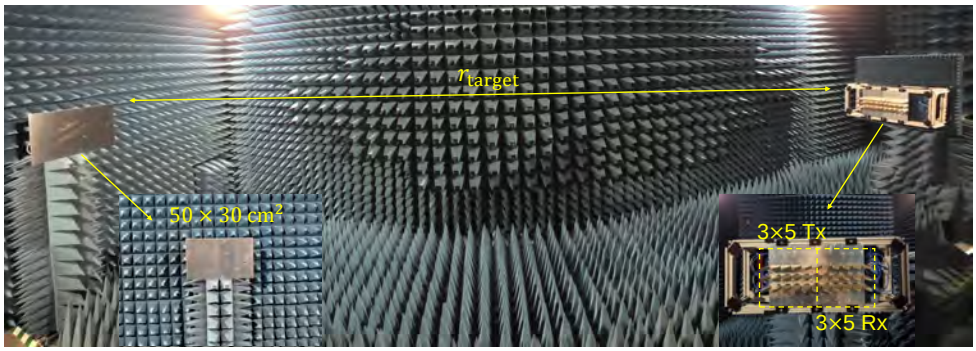


Figure 3.11: Full-duplex radar measurement configuration using the previously developed separate-aperture 3×5 Vivaldi Tx/Rx arrays, the RFSoC back-end, and an aluminum plate target. The configuration is extended from the IBFD testbed described in Section 3.1 by introducing the FMCW radar waveform and target (adapted from [59]).

The radar experiment differs from the communication experiments in an important respect. The objective is no longer to optimize Tx and Rx beamformers for a communication link jointly. Instead, the Tx excitation is designed to maximize the desired target-echo response while satisfying a prescribed Tx–Rx isolation constraint. The resulting Tx excitation is restricted to the low-coupling spatial subspace identified from the measured Tx–Rx coupling matrix. This allows SI to be suppressed at the antenna level while retaining sufficient transmit radiation toward the target [59].

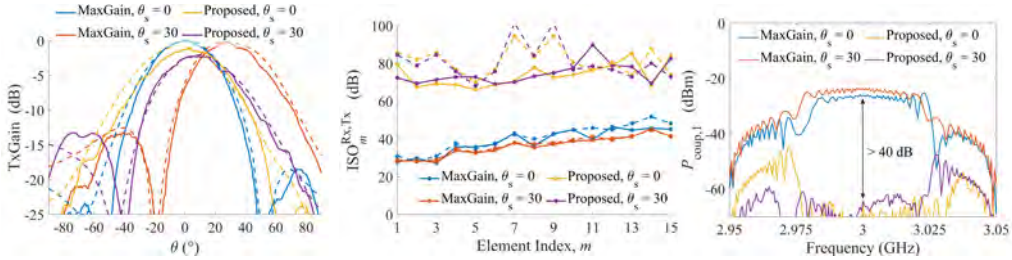
The antenna arrays, RFSoC platform, synchronization procedure, and coupling-matrix measurement methodology have already been established in the preceding sections and are therefore not repeated here. The following subsections focus only on the radar-specific configuration and experimental results.

Radar Measurement Configuration and SI Mitigation

Measurement Configuration: The FD-radar experiment uses the same separate-aperture 3×5 Vivaldi Tx and Rx arrays and RFSoC-based measurement platform described in Section 3.1. A triangular FMCW waveform centered at $f_c = 3$ GHz with a bandwidth of 100 MHz is used. No external PA or LNA is used in the radar measurements.

A 30×50 cm^2 aluminum plate is used as the radar target and is placed inside the anechoic chamber. The target provides a well-defined reflecting surface that enables the effect of SI suppression on the recovered FMCW range response to be evaluated. Three measurement configurations are considered. The first configuration corresponds to broadside operation with the target located at 4.6 m. This distance represents the chamber-limited measurement range used in the experiment. The second configuration uses a 30° off-boresight target direction with a target range of 3.8 m. This configuration is obtained by rotating the testbed relative to the target while maintaining the same propagation environment. The third configuration corresponds to broadside operation with the target placed at 3 m, representing the minimum far-field distance used in the experiment. Range profiles are obtained by matched filtering with the known FMCW waveform after the corresponding Tx and Rx beamforming weights are applied.

SI Suppression: Before evaluating target detection, the SI suppression provided by the constrained Tx beamformer is experimentally characterized. The 3 GHz eigenvalue spectrum



(a) (b) (c)

Figure 3.12: (a) Normalized Tx array radiation pattern at E-plane for 0° and 30° scan angles (simulation: dashed, measurement: solid); (b) Per-element Rx isolation at 3 GHz with all Tx elements active (simulation: dashed, measurement: solid); (c) Measured maximum coupled Rx power ($m = 1$) over a 100 MHz band.

(Figure 3.8) analysis presented previously provides the spatial basis for identifying the low-coupling Tx subspace. The same measured coupling characteristics are therefore used to construct the radar Tx beamformer.

Figure 3.12(a) compares the normalized Tx radiation patterns obtained using the max-Txgain beamformer and the proposed constrained solution for broadside and 30° steering. The proposed beamformer preserves the desired beam directions in both configurations, demonstrating that the isolation constraint does not prevent the array from steering toward the target. The main effect of the constraint is a reduction in peak Tx gain. Depending on the steering direction, the constrained solution results in approximately 1–4.3 dB reduction relative to the maxTxgain beamformer. This reduction represents the spatial cost of excluding strongly coupled excitation modes from the Tx solution. Importantly, the reduction is limited, meaning that a substantial portion of the desired radiation capability remains available after the isolation constraint is imposed.

The corresponding Rx isolation at 3 GHz is shown in Figure 3.12(b). With maxTxgain transmission, the measured isolation is approximately 30–45 dB. When the Tx excitation is constrained according to $\kappa = 45$ dB, the measured per-element isolation increases to approximately 66–88 dB.

The frequency dependence of the SI suppression is shown in Figure 3.12(c). Although the beamformer is designed using the coupling matrix at the center frequency, the measured maximum coupled Rx power remains substantially reduced over the complete 100 MHz FMCW bandwidth. More than 40 dB reduction in the maximum coupled Rx power is maintained across the measured band. This behavior indicates that the dominant Tx–Rx coupling subspace varies only moderately over the 3.3% fractional bandwidth considered in the experiment. Consequently, the center-frequency beamformer remains effective over the FMCW bandwidth without requiring a separate frequency-dependent beamformer at every frequency point. This is important for practical FMCW operation because it allows the spatial SI suppression to be implemented with a fixed Tx excitation over the radar sweep.

FMCW Target Detection

The ultimate objective of the FD-radar experiment is to determine whether the reduction in direct Tx–Rx coupling allows the target echo to be recovered. Figure 3.13 compares the simulated and measured FMCW range profiles obtained with conventional maxTxgain

and proposed constrained Tx beamforming. With conventional transmission, the strong direct Tx–Rx coupling produces a dominant near-zero-range SI peak that masks the target response, preventing reliable target detection. In contrast, the proposed constrained Tx beamformer suppresses the SI while retaining sufficient radiation toward the target, allowing the target echo to emerge clearly from the range profile.

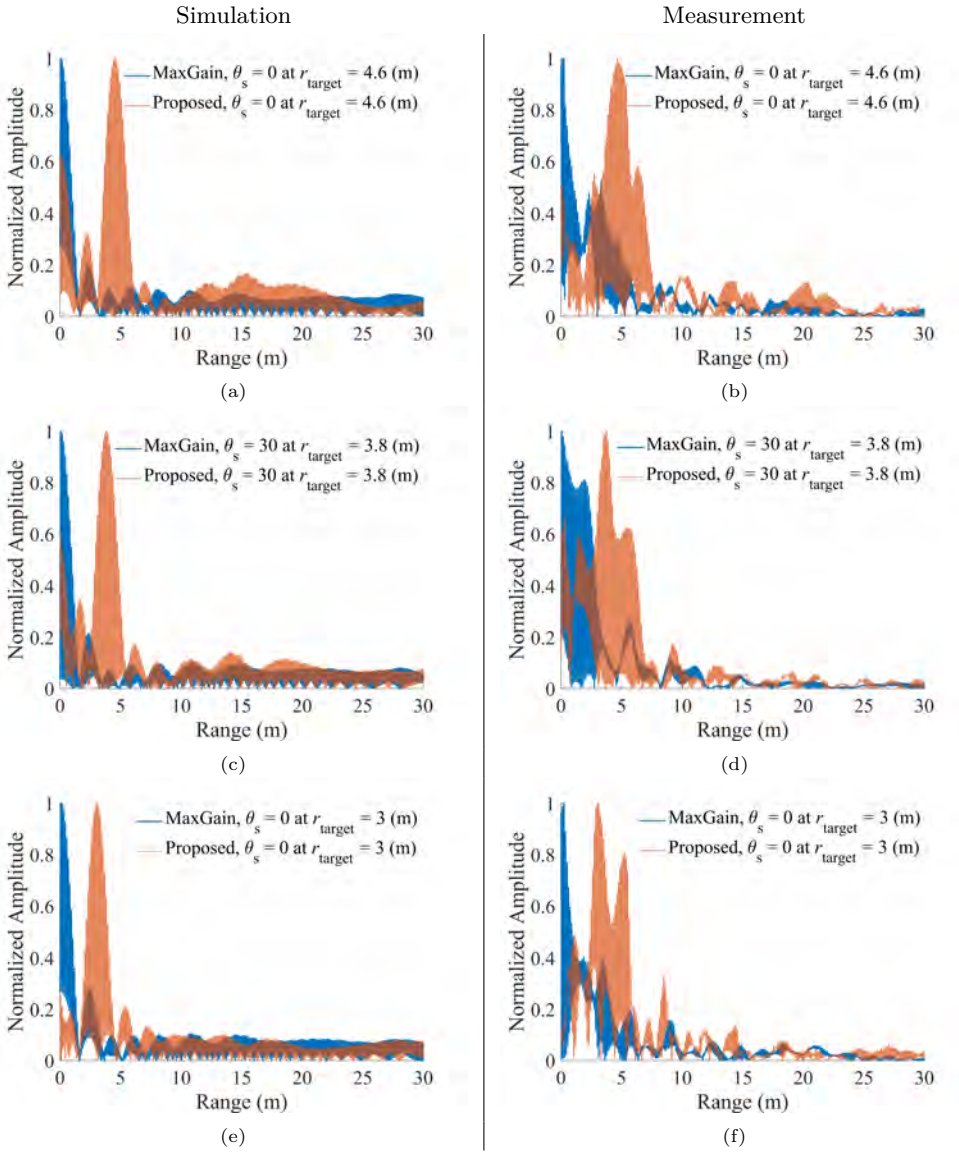


Figure 3.13: Simulated and measured FMCW range profiles obtained with conventional maximum-gain and proposed constrained Tx beamforming ($\kappa = 45$ dB). Results are shown for broadside operation at $r_{\text{target}} = 4.6$ m (a,b), 30° off-boresight operation at $r_{\text{target}} = 3.8$ m (c,d), and broadside operation at $r_{\text{target}} = 3$ m (e,f).

This behavior is observed for all three measurement configurations: broadside operation at $r_{\text{target}} = 4.6$ m, 30° off-boresight operation at $r_{\text{target}} = 3.8$ m, and broadside operation at $r_{\text{target}} = 3$ m. In each case, the target range is correctly recovered with the constrained beamformer, whereas the target remains masked by the SI under conventional maximum-gain transmission. The reduction in target-echo power is relatively small, indicating that the low-coupling Tx subspace retains sufficient spatial DoF for target illumination.

The measured and simulated range profiles exhibit consistent SI-suppression and target-detection trends. The remaining differences are mainly attributed to RFSoC DAC/ADC nonlinearities, residual calibration errors, and the finite receiver dynamic range, which limits the measurable suppression at the highest isolation levels. Overall, the results demonstrate that the antenna-level reduction of direct Tx–Rx coupling translates into a practical improvement in FMCW target detectability, providing experimental validation of the sensing-oriented beamforming approach presented in [59].

3.4 Chapter Summary

This chapter presented the development and experimental validation of the proposed integrated IBFD system. A 3×5 Vivaldi Tx/Rx antenna testbed was integrated with the ZCU216 RFSoC platform, and the required measurement, synchronization, calibration, and coupling-characterization procedures were established. The proposed beamforming framework was experimentally validated for both SU- and MU-MIMO operation, demonstrating substantial Tx–Rx isolation while preserving the desired beamforming performance. Finally, the framework was extended to an FD-radar scenario, where the constrained Tx beamformer significantly reduced direct Tx–Rx coupling and enabled reliable FMCW target detection. These results experimentally confirm the effectiveness of the proposed SI-based beamforming approach for both communication and sensing applications.

CHAPTER 4

Machine-Learning-Assisted Synthesis of Full-Duplex MIMO Antennas

Antenna-level isolation is a key aspect of the in-band full-duplex multi-input multi-output (FD-MIMO) architecture considered, since Tx–Rx coupling directly contributes to the self-interference (SI) channel. Increasing the intrinsic isolation between the antenna ports therefore reduces the SI that the subsequent cancellation and beamforming stages must handle.

Conventional antenna design relies on repeated full-wave electromagnetic simulations, which become computationally demanding when the antenna topology, rather than only a few geometrical parameters, is being optimized. Machine learning (ML) offers an alternative: a fast surrogate of the electromagnetic response allows a large number of candidate geometries to be evaluated without a full-wave simulation for each one.

This chapter presents an ML-assisted methodology for synthesizing compact four-port antennas with enhanced inter-port isolation. It combines a symmetry-constrained pixel representation, a convolutional neural network (CNN) surrogate, and a binary genetic algorithm (GA), and is based on our previously published work [60]. The emphasis here is on its role as an SI-mitigation technique within the FD-MIMO architecture.

4.1 Symmetry-Constrained Antenna Representation

The patch antenna topology is represented using a binary pixel grid. The physical conducting region has dimensions of 34×34 mm^2 and is represented by a 17×17 binary matrix, where each pixel corresponds to a 2×2 mm^2 region. A binary variable is defined as $x_{m,n} \in \{0, 1\}$, where $x_{m,n} = 1$ represents a metallic region and $x_{m,n} = 0$ represents air.

To reduce the design space and promote consistent multi-port behavior, fourfold rotational symmetry is imposed. Only an 8×9 seed pattern is independently generated, while the complete 17×17 topology is obtained through rotations of the seed pattern by 90°, 180°, and 270°. The antenna topology and the symmetry-generation procedure are shown in Figures 4.1 and 4.2, respectively. The symmetry constraint reduces the number of independent topology variables while ensuring rotationally consistent behavior among the four ports. Electrically disconnected metal regions are excluded from the generated designs.

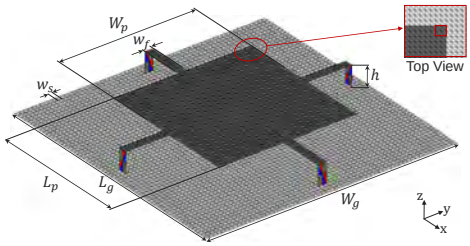


Figure 4.1: Pixel-based representation with labeled feed and ground dimensions: $w_s = 1$ mm, $w_f = 2$ mm, $h = 3$ mm, $W_p = L_p = 34$ mm, and $W_g = L_g = 48$ mm.

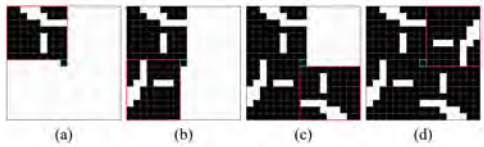


Figure 4.2: Generation of the fourfold rotationally symmetric antenna topology from an 8×9 seed pattern through successive $90°$ rotations. The green inset highlights the central index, determined by the element at position $(8, 9)$ in the seed matrix.

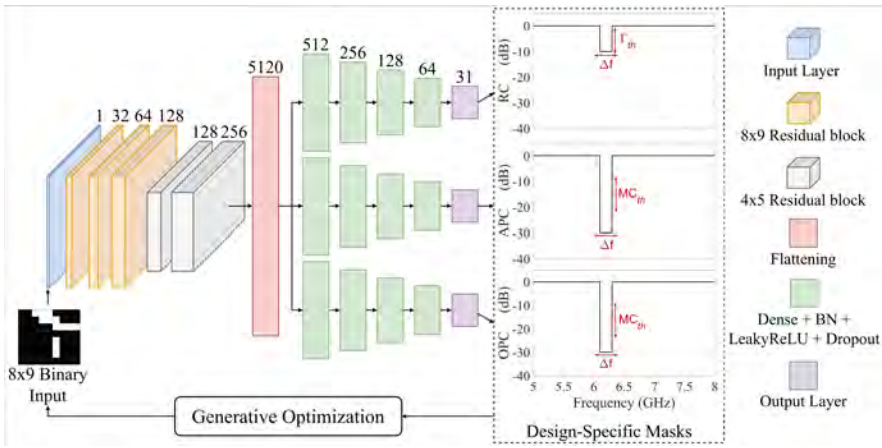


Figure 4.3: Generalized CNN for predicting RC, APC, and OPC from 8×9 seed patterns. A shared convolutional encoder extracts spatial features that are mapped to three task-specific output branches. The trained surrogate enables rapid evaluation of candidate antennas during generative optimization [60].

4.2 Surrogate Model

Due to the fourfold symmetry and reciprocity property, the complete 4×4 scattering matrix does not need to be independently predicted. In particular, $S_{11} = S_{22} = S_{33} = S_{44}$, $S_{21} = S_{32} = S_{43} = S_{14}$, and $S_{31} = S_{42}$. The remaining terms follow from reciprocity, $S_{ij} = S_{ji}$. Consequently, the electromagnetic behavior can be represented by three independent responses of S_{11}, S_{21}, and S_{31} which are referred to as the reflection coefficient (RC), adjacent-port coupling (APC), and opposite-port coupling (OPC), respectively. The responses are evaluated from 5 to 8 GHz using 31 frequency samples. A large database of approximately 1.6 million symmetry-constrained antenna topologies was generated using an in-house MoM solver [65] and divided into training, validation, and test sets.

The CNN surrogate uses a shared convolutional encoder followed by three task-specific output branches, as illustrated in Figure 4.3. The shared encoder extracts spatial features from the binary topology, while the three output branches predict the frequency-dependent RC, APC, and OPC responses. Each block contains 2D convolutional layers with batch nor-

malization (BN) and Leaky Rectified Linear Unit (LeakyReLU) activations. The resulting surrogate achieves test-set mean squared error (MSE) values of 8.21×10^{-4}, 2.25×10^{-4}, and 3.32×10^{-4} for RC, APC, and OPC, respectively [60].

4.3 Generative Antenna Optimization

After training, the CNN is incorporated into a binary elitist GA to search the 8×9 topology space. For each candidate antenna, the CNN rapidly predicts the frequency-dependent S-parameters, which are then used to evaluate the design objectives as shown in Figure 4.3.

The main advantage of this approach is the reduction in computational cost. Once trained, the CNN can evaluate a population of 512 candidate antennas in approximately 17 ms, whereas a conventional MoM simulation requires approximately 2.17 s per antenna. Thus, the computationally expensive full-wave simulations are mainly required during the offline dataset-generation stage, while the topology search is performed using fast ML inference. This enables large-scale exploration of antenna topologies that would be impractical using conventional simulation-driven optimization.

4.4 Validation

Three optimized four-port antennas were fabricated to validate the proposed methodology. The designs were optimized for different frequency ranges and isolation requirements. The fabricated prototypes are shown in Figure 4.4.

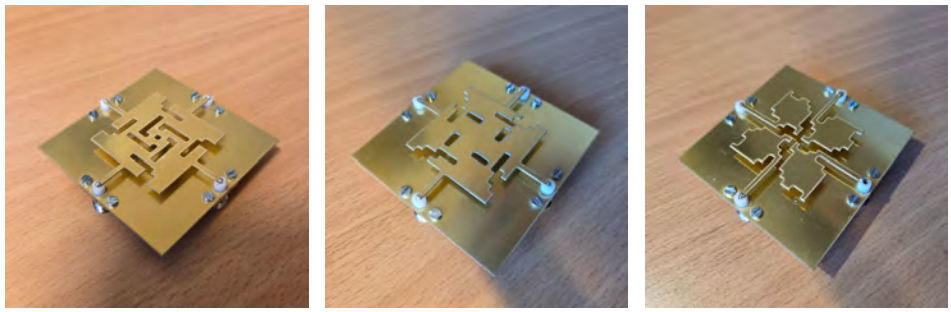
The simulated, CNN-predicted, and measured S-parameters show good agreement (see Figure 4.5), confirming the capability of the surrogate model to guide the antenna synthesis process. In particular, Antenna-A and Antenna-B achieved approximately 25 dB and 28.7 dB isolation over fractional bandwidths of approximately 3.8% and 3.5%, respectively. The optimized antennas also maintained good radiation performance, with measured peak realized gains between approximately 7.5 and 8.25 dBi. The simulated total efficiencies exceeded 90% for all three designs. These results demonstrate that high isolation can be obtained without introducing additional decoupling structures such as defected ground structures or resonators [60].

The proposed multi-port antenna achieves high isolation through strong modal confinement in the patch geometry, where stepped edges and asymmetrical shaping suppress global resonances and favor spatially localized current distributions,[1] as shown in Figure 4.6. As a result, the currents at excited and non-excited matched-terminated ports are rather different in magnitude ($\sim$ 25 dB) and similar to the measured port isolation levels.

4.5 Chapter Remarks

The ML-assisted antenna synthesis presented in this chapter provides an effective antenna-level approach for reducing SI in FD-MIMO systems. By lowering the intrinsic coupling between the Tx and Rx ports, the resulting antenna design reduces the SI level that must be suppressed by subsequent cancellation stages. Thus, the proposed approach complements the Tx/Rx beamforming and cancellation techniques developed in the previous chapters, forming the antenna-level foundation of the overall FD-MIMO SI-mitigation strategy.

[1] Note that, even if $\int \mathbf{J}_i^* \cdot \mathbf{J}_j \, dS = 0$ for $i \neq j$, spatially non-overlapping currents may still couple if $\int \mathbf{J}_i^* \cdot \mathbf{E}(\mathbf{J}_j) \, dS \neq 0$. Mutual coupling can be more directly measured by the overlap of embedded element fields [69].



(a) (b) (c)

Figure 4.4: Fabricated quad-port antennas: (a) antenna-A, (b) antenna-B, and (c) antenna-C.

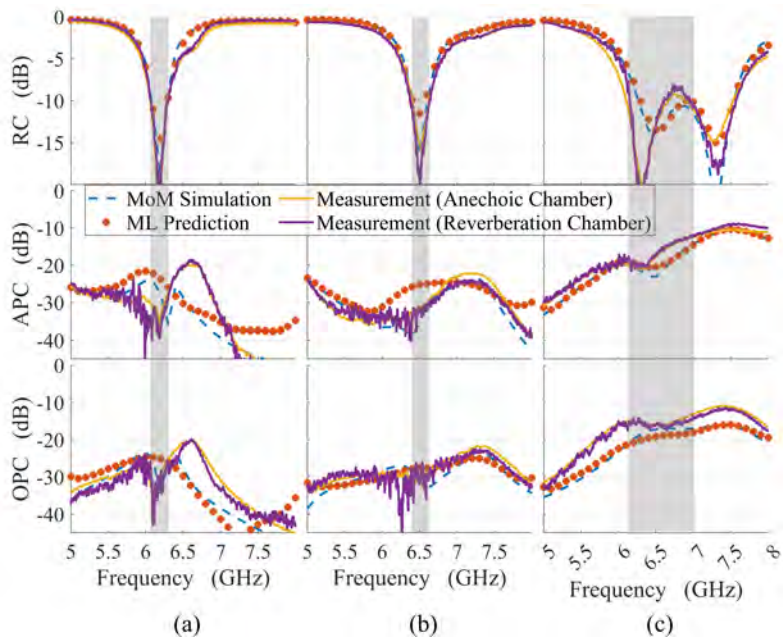


Figure 4.5: Simulated, CNN-predicted, and measured S-parameters of (a) antenna-A, (b) antenna-B, (c) antenna-C.

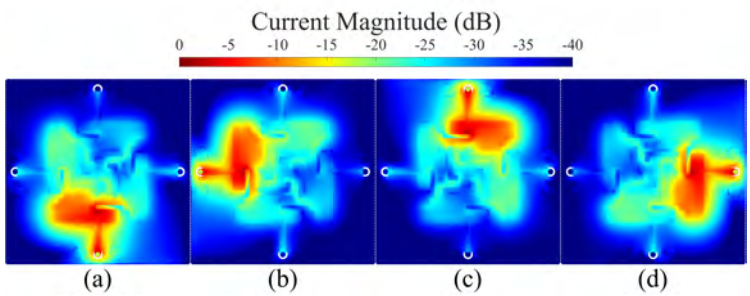


Figure 4.6: Normalized surface-current distributions for the four-port antenna when each port is excited individually.

CHAPTER 5

Summary of included papers

This chapter provides a summary of the included papers.

5.1 Paper A

Mustafa Ayebe, Johan Malmström, Sten E. Gunnarson, Henrik Holter, Marianna Ivashina, Carlo Bencivenni, and Rob Maaskant
Systematic Self-Interference Mitigation In Full Duplex Antenna Arrays Via Transmit Beamforming
2023 IEEE Int. Conf. Electromagn. Adv. Appl. (ICEAA),
Venice, Italy, 2023.
©IEEE *DOI: 10.1109/ICEAA57318.2023.10297706.*

The paper derives an optimal antenna array excitation vector to maximize array gain in a given direction, while directly controling the self-interference coupling power to the receive side to exceed a certain maximum threshold level. This is very useful for in-band full-duplex systems where the hardware complexity for self-interference mitigation must be minimized. Numerical results are shown for a 25-element transmit and receive setup with specific spacing.

5.2 Paper B

Mustafa Ayebe, Rob Maaskant, Johan Malmström, Sten E. Gunnarson, Henrik Holter, and Marianna Ivashina
3D-printed Silver-coated Vivaldi Array With Integrated Coaxial Probe Feeding
2024 IEEE Int. Symp. Antennas Propag. INC/USNC-URSI Radio Sci. Meeting (AP-S/INC-USNC-URSI),
Firenze, Italy, 2024.
©IEEE *DOI: 10.1109/AP-S/INC-USNC-URSI52054.2024.10686495.*

A Vivaldi antenna array for 3–6 GHz phased array applications is designed with a novel coaxial probe feed. Simulated active reflection coefficients stay below -10 dB for $\pm 60^\circ$ E-plane and $\pm 50^\circ$ H-plane scans. Measured results for a 1×5 array agree with simulations, validating the infinite array model and probe feed design. The 3D-printed, silver-coated

fabrication enables rapid, cost-effective prototyping.

5.3 Paper C

Mustafa Ayebe, Rob Maaskant, Sten E. Gunnarson, Johan Malmström, Marianna Ivashina, and Henrik Holter
Joint Tx-Rx Beamforming for Optimal Gain and Self Interference Mitigation in In-Band Full-Duplex Arrays: Theory, Figures of Merit, and Validation
IEEE Antennas Wireless Propag. Lett. (2025).
Recipient of the IEEE AP-S Acharya Jagadish Chandra Bose Paper Award.
©IEEE DOI: 10.1109/LAWP.2025.3534882.

We present a joint transmit (Tx) and receive (Rx) beamforming method for in-band full-duplex antenna systems, addressing self-interference (SI) leakage and non-linear gain compression in the receiver's low-noise amplifiers (LNAs). Unlike conventional methods that handle Tx and Rx beamforming independently, our approach maximizes Tx gain while controlling SI at the LNAs input to maintain linearity and further suppresses residual SI at the Rx output—validated using a commercial radio frequency system-on-chip evaluation board and a 3×5 Tx/Rx Vivaldi antenna array.

5.4 Paper D

Mustafa Ayebe, et al.
In-Band Full-Duplex Antenna Beamforming and Synchronization for Self-Interference Mitigation: Multi-Tile RFSoC Testbed Design and Deployment
2025 19th Eur. Conf. Antennas Propag. (EuCAP),
Stockholm, Sweden, 2025.
©IEEE DOI: 10.23919/EuCAP63536.2025.10999554.

This paper presents an in-band full-duplex communication and sensing testbed using digital beamforming on the Xilinx ZCU216 RFSoC platform with 16 digital-to-analog converters and 16 analog-to-digital converters (14-bit) across four tiles. Key challenges include phase synchronization across RFSoC tiles and self-interference (SI) mitigation due to mutual coupling between transmit (Tx) and receive (Rx) antenna arrays. To address these, we used Tx beamforming for maximum gain and Rx beamforming to enhance the signal-to-SI ratio. Our setup includes two 1×5 Vivaldi antenna arrays (3–6 GHz) and a multi-tile synchronization framework. Experimental results show over 80 dB SI suppression with half-wavelength spacing (@6 GHz) between Tx and Rx arrays, demonstrating the potential of the testbed for 6G communication and radar sensing.

5.5 Paper E

Mustafa Ayebe, Rob Maaskant, Marianna Ivashina, Henrik Holter, and Johan Malmström
Generative Deep-Learning Design of Single- and Dual-Polarized Four-Port MIMO Antennas for Full-Duplex Communication
IEEE Antennas Wireless Propag. Lett. (2026).
©IEEE DOI: 10.1109/LAWP.2026.3667625.

This work presents a machine-learning-driven framework for designing single- and dual-polarized, four-port MIMO antennas for in-band full-duplex operation. A symmetry-constrained, pixel-based layout enables efficient exploration of the design space. A multi-task convolutional neural network surrogate is trained to jointly predict return loss and multi-port

coupling from symmetric pixel layouts, accurately modeling the amplitude of the 4×4 S-parameter matrix across 5–8 GHz. By embedding this surrogate within a binary genetic algorithm, the framework synthesizes antenna layouts that simultaneously achieve impedance matching and high inter-port isolation across the operating band.

5.6 Paper F

Mustafa Ayebe, Rob Maaskant, Bo Göransson, and Henrik Holter
Transmit and Receive Beamforming for In-Band Full-Duplex MU-MIMO under Self-Interference Constraints with Measurement-Based Validation
IEEE Open J. Antennas Propag. (2026).
©IEEE DOI: 10.1109/OJAP.2026.3715376.

This paper presents a measurement-based transmit and receive beamforming framework for in-band full-duplex multi-user MIMO systems. The proposed approach mitigates self-interference by exploiting measured coupling characteristics to constrain transmit beamforming and applying subspace projection at the receiver, while preserving the spatial degrees of freedom required for multi-user communication. The framework is validated through full-wave simulations and experimental measurements using a hardware testbed.

5.7 Paper G

Mustafa Ayebe, Rob Maaskant, Marianna Ivashina, Henrik Holter, and Andreas Wikström
Antenna-level Self-Interference Suppression in Full-Duplex Radar via Transmit Beamforming
IEEE Antennas Wireless Propag. Lett. (2026).
©IEEE DOI: 10.1109/LAWP.2026.3720787.

This letter proposes a transmit beamforming method for antenna-level self-interference suppression in full-duplex radar by constraining the transmit excitation to a low-coupling modal subspace while maximizing the received target echo. Experimental validation using an RFSoC-based equency-modulated continuous-wave radar with closely spaced 3×5 Vivaldi arrays successful recovery of target echoes otherwise masked under conventional maximum-gain transmission.

5.8 Paper H

Mustafa Ayebe, Rob Maaskant, and Marianna Ivashina
Self-Interference–Constrained Transmit Beamforming in Interleaved and Displaced In-Band Full-Duplex Arrays: Gain and Isolation Trade–Offs
2026 IEEE Int. Symp. Antennas Propag. USNC-URSI Radio Sci. Meeting (AP-S/URSI),
Detroit, MI, USA, 2026.
©IEEE DOI: 10.1109/AP-S/USNC-URSI60190.2026.11674852.

This paper investigates self-interference-constrained transmit beamforming for interleaved and vertically displaced in-band full-duplex antenna arrays. Full-wave simulations quantify the trade-off between transmit array gain and required Tx–Rx isolation for varying array geometries. Results show that strong lateral interleaving significantly increases gain loss under stringent isolation constraints, whereas vertical separation effectively reduces coupling and preserves high transmit gain. The study provides practical design guidelines for jointly optimizing array geometry and beamforming in compact IBFD systems.

CHAPTER 6

Concluding Remarks and Future Research Directions

This thesis has investigated SI mitigation in IBFD wireless systems from an integrated antenna and signal-processing perspective. The main contribution is the formulation of SI mitigation as a constrained optimization problem, where the required Tx-to-Rx isolation is achieved without unnecessarily forcing the coupling to zero. This enables a more effective trade-off between SI suppression, Tx array gain, and the available DoF for communication and sensing. The results demonstrate the applicability of this approach to antenna-level isolation, Tx-Rx beamforming, multi-user communication, and full-duplex sensing. Overall, the thesis establishes that effective SI mitigation requires a joint approach involving antenna design, beamforming, and signal processing.

Several directions remain open for future research. A first direction is the extension of the proposed optimization framework to **wider-band and adaptive operation**. The results obtained for the 100 MHz FMCW radar demonstrate that a solution designed at the center frequency can maintain effective SI suppression over a finite operating bandwidth. Future work can build on this result by investigating the bandwidth limits of the center-frequency design and identifying the conditions under which frequency-dependent subspaces or joint spatio-temporal precoding become necessary. In practical systems, the required suppression must also be maintained under channel variations caused by moving objects, structural changes, temperature variations, and hardware drift. Combining bandwidth-based optimization with robust and adaptive beamforming could therefore extend the demonstrated approach to wider-band and dynamically varying IBFD systems.

A second direction concerns **joint RF and digital SI cancellation with beamforming**. Beamforming can suppress the dominant linear SI component before it reaches the receiver front end, allowing subsequent RF and digital cancellation stages to focus on residual interference caused by nonlinear PA distortion, phase noise, and dynamic multipath components. Such a hierarchical architecture could provide a more scalable solution for practical IBFD transceivers. In parallel, the machine-learning-based antenna synthesis developed in this thesis could be extended toward hardware-in-the-loop optimization, where measured RF responses are incorporated into the learning process to account for fabrication tolerances, hardware variations, and environmental effects.

A further direction is the investigation of **non-reciprocal and shared-aperture an-**

tenna architectures. In reciprocal systems, electromagnetic reciprocity imposes constraints on the Tx and Rx responses, which can limit their independent optimization in shared-aperture configurations. Non-reciprocal antennas could potentially provide greater freedom to shape the Tx and Rx spatial responses independently, enabling SI reduction while preserving the desired communication or sensing beam. Integrating such architectures with the proposed constrained beamforming framework could therefore provide additional DoF for SI mitigation and reduce the reliance on signal-processing techniques.

Another important direction is the extension toward **near-field ISAC**. At mmWave and sub-THz frequencies, communication users and sensing targets may operate in the radiative near-field, where spherical wavefronts and focusing effects become important. Extending the proposed SI mitigation framework to near-field channels could enable the joint optimization of SI suppression, communication beams, and sensing focal points. This would provide a natural pathway from the IBFD communication and radar concepts investigated in this thesis toward full-duplex ISAC systems.

Overall, these directions point toward future IBFD systems in which antenna design, RF processing, beamforming, and signal processing are jointly optimized. Such an integrated approach can reduce the SI burden before it reaches the receiver front end while preserving the resources required for communication and sensing, providing a promising foundation for future full-duplex ISAC architectures.

References

[1] M. Mohammadi, Z. Mobini, D. Galappaththige, and C. Tellambura, "A comprehensive survey on full-duplex communication: Current solutions, future trends, and open issues," *IEEE Commun. Surveys Tuts.*, vol. 25, no. 4, pp. 2190–2244, 2023.

[2] D. Kim, H. Lee, and D. Hong, "A survey of in-band full-duplex transmission: From the perspective of PHY and MAC layers," *IEEE Commun. Surveys Tuts.*, vol. 17, no. 4, pp. 2017–2046, 2015.

[3] B. Smida, A. Sabharwal, G. Fodor, G. C. Alexandropoulos, H. A. Suraweera, and C.-B. Chae, "Full-duplex wireless for 6G: Progress brings new opportunities and challenges," *IEEE J. Sel. Areas Commun.*, vol. 41, no. 9, pp. 2729–2750, 2023.

[4] S. A. Hassani et al., "In-band full-duplex radar-communication system," *IEEE Syst. J.*, vol. 15, no. 1, pp. 1086–1097, 2020.

[5] G. C. Alexandropoulos, M. A. Islam, and B. Smida, "Full-duplex massive multiple-input, multiple-output architectures: Recent advances, applications, and future directions," *IEEE Veh. Technol. Mag.*, vol. 17, no. 4, pp. 83–91, 2022.

[6] S. A. Hassani, B. van Liempd, A. Bourdoux, F. Horlin, and S. Pollin, "Joint in-band full-duplex communication and radar processing," *IEEE Syst. J.*, vol. 16, no. 2, pp. 3391–3399, 2021.

[7] K. E. Kolodziej, B. T. Perry, and J. S. Herd, "In-band full-duplex technology: Techniques and systems survey," *IEEE Trans. Microw. Theory Techn.*, vol. 67, no. 7, pp. 3025–3041, 2019.

[8] B. Smida, R. Wichman, K. E. Kolodziej, H. A. Suraweera, T. Riihonen, and A. Sabharwal, "In-band full-duplex: The physical layer," *Proc. IEEE*, vol. 112, no. 5, pp. 433–462, 2024.

[9] Anthropic, *Claude Sonnet 5.5 (large language model)*, [Online]. Available: `https://claude.ai`, 2026.

[10] Y. Kim, H.-J. Moon, H. Yoo, B. Kim, K.-K. Wong, and C.-B. Chae, "A state-of-the-art survey on full-duplex network design," *Proc. IEEE*, vol. 112, no. 5, pp. 463–486, 2024.

[11] T. Wild, V. Braun, and H. Viswanathan, "Joint design of communication and sensing for beyond 5G and 6G systems," *IEEE Access*, vol. 9, pp. 30 845–30 857, 2021.

[12] D. K. P. Tan et al., "Integrated sensing and communication in 6G: Motivations, use cases, requirements, challenges and future directions," in *IEEE Int. Online Symp. Joint Commun. Sens. (JC&S)*, 2021, pp. 1–6.

[13] H. Ju and R. Zhang, "Optimal resource allocation in full-duplex wireless-powered communication network," *IEEE Trans. Commun.*, vol. 62, no. 10, pp. 3528–3540, 2014.

[14] E. Lagunas et al., "Full-duplex techniques for satellite communications: Feasibility analysis and roadmap," *IEEE Open J. Commun. Soc.*, vol. 6, pp. 2130–2151, 2025.

[15] A. Kiayani et al., "Adaptive nonlinear RF cancellation for improved isolation in simultaneous transmit–receive systems," *IEEE Trans. Microw. Theory Techn.*, vol. 66, no. 5, pp. 2299–2312, 2018.

[16] D. Korpi, T. Riihonen, V. Syrjälä, L. Anttila, M. Valkama, and R. Wichman, "Full-duplex transceiver system calculations: Analysis of ADC and linearity challenges," *IEEE Trans. Wireless Commun.*, vol. 13, no. 7, pp. 3821–3836, 2014.

[17] M. Duarte and A. Sabharwal, "Full-duplex wireless communications using off-the-shelf radios: Feasibility and first results," in *Conf. Rec. 44th Asilomar Conf. Signals, Syst. Comput.*, 2010, pp. 1558–1562.

[18] B. P. Day, A. R. Margetts, D. W. Bliss, and P. Schniter, "Full-duplex bidirectional MIMO: Achievable rates under limited dynamic range," *IEEE Trans. Signal Process.*, vol. 60, no. 7, pp. 3702–3713, 2012.

[19] M. B. Dastjerdi, S. Jain, N. Reiskarimian, A. Natarajan, and H. Krishnaswamy, "Analysis and design of a full-duplex two-element MIMO circulator-receiver with high TX power handling exploiting mimo rf and shared-delay baseband self-interference cancellation," *IEEE J. Solid-State Circuits*, vol. 54, no. 12, pp. 3525–3540, 2019.

[20] E. Everett, A. Sahai, and A. Sabharwal, "Passive self-interference suppression for full-duplex infrastructure nodes," *IEEE Trans. Wireless Commun.*, vol. 13, no. 2, pp. 680–694, 2014.

[21] H. Nawaz and I. Tekin, "Compact dual-polarised microstrip patch antenna with high interport isolation for 2.5 GHz in-band full-duplex wireless applications," *IET Microw. Antennas Propag.*, vol. 11, no. 7, pp. 976–981, 2017.

[22] M. Heino, S. N. Venkatasubramanian, C. Icheln, and K. Haneda, "Design of wave-traps for isolation improvement in compact in-band full-duplex relay antennas," *IEEE Trans. Antennas Propag.*, vol. 64, no. 3, pp. 1061–1070, 2015.

[23] P. V. Prasannakumar, M. A. Elmansouri, and D. S. Filipovic, "Wideband decoupling techniques for dual-polarized bi-static simultaneous transmit and receive antenna subsystem," *IEEE Trans. Antennas Propag.*, vol. 65, no. 10, pp. 4991–5001, 2017.

[24] S. N. Venkatasubramanian, L. Li, A. Lehtovuori, C. Icheln, and K. Haneda, "Impact of using resistive elements for wideband isolation improvement," *IEEE Trans. Antennas Propag.*, vol. 65, no. 1, pp. 52–62, 2016.

[25] Y.-N. Chen, C. Ding, H. Zhu, and Y. Liu, "A±45°-polarized antenna system with four isolated channels for in-band full-duplex (ibfd)," *IEEE Trans. Antennas Propag.*, 2023.

[26] K. Kolodziej, P. Hurst, A. Fenn, and L. Parad, "Ring array antenna with optimized beamformer for simultaneous transmit and receive," in *Proc. IEEE Int. Symp. Antennas Propag.*, 2012, pp. 1–2.

[27] M. A. Elmansouri, A. J. Kee, and D. S. Filipovic, "Wideband antenna array for simultaneous transmit and receive (STAR) applications," *IEEE Antennas Wireless Propag. Lett.*, vol. 16, pp. 1277–1280, 2016.

[28] T. Snow, C. Fulton, and W. J. Chappell, "Transmit–receive duplexing using digital beamforming system to cancel self-interference," *IEEE Trans. Microw. Theory Techn.*, vol. 59, no. 12, pp. 3494–3503, 2011.

[29] M. Ayebe, R. Maaskant, J. Malmström, S. E. Gunnarson, H. Holter, and M. Ivashina, "Evaluation of the self-interference cancellation limits of full-duplex antenna arrays using zynq ultrascale+ RF system-on-chip board," in *IEEE Int. Symp. Phased Array Syst. Technol. (ARRAY)*, 2024, pp. 1–4.

[30] A. T. Wegener and W. J. Chappell, "Coupled antenna scheme using filter design techniques and tunable resonators to show simultaneous transmit and receive," in *IEEE MTT-S Int. Microw. Symp. Dig.*, 2013, pp. 1–4.

[31] M. E. Knox, "Single antenna full duplex communications using a common carrier," in *Proc. IEEE Wireless Microw. Technol. Conf. (WAMICON)*, 2012, pp. 1–6.

[32] J. I. Choi, M. Jain, K. Srinivasan, P. Levis, and S. Katti, "Achieving single channel, full duplex wireless communication," in *Proc. ACM Int. Conf. Mobile Comput. Netw. (MobiCom)*, 2010, pp. 1–12.

[33] M. Duarte, C. Dick, and A. Sabharwal, "Experiment-driven characterization of full-duplex wireless systems," *IEEE Trans. Wireless Commun.*, vol. 11, no. 12, pp. 4296–4307, 2012.

[34] D. Bharadia, E. McMilin, and S. Katti, "Full duplex radios," in *Proc. ACM SIGCOMM*, 2013, pp. 375–386.

[35] M. Duarte et al., "Design and characterization of a full-duplex multiantenna system for WiFi networks," *IEEE Trans. Veh. Technol.*, vol. 63, no. 3, pp. 1160–1177, 2013.

[36] S. B. Venkatakrishnan, E. A. Alwan, and J. L. Volakis, "Wideband RF self-interference cancellation circuit for phased array simultaneous transmit and receive systems," *IEEE Access*, vol. 6, pp. 3425–3432, 2018.

[37] D.-J. van den Broek, E. A. Klumperink, and B. Nauta, "An in-band full-duplex radio receiver with a passive vector modulator downmixer for self-interference cancellation," *IEEE J. Solid-State Circuits*, vol. 50, no. 12, pp. 3003–3014, 2015.

[38] H. Krishnaswamy and G. Zussman, "1 chip 2x the bandwidth," *IEEE Spectr.*, vol. 53, no. 7, pp. 38–54, 2016.

[39] Y. Liu, X. Quan, W. Pan, and Y. Tang, "Digitally assisted analog interference cancellation for in-band full-duplex radios," *IEEE Commun. Lett.*, vol. 21, no. 5, pp. 1079–1082, 2017.

[40] T. Riihonen, S. Werner, and R. Wichman, "Mitigation of loopback self-interference in full-duplex MIMO relays," *IEEE Trans. Signal Process.*, vol. 59, no. 12, pp. 5983–5993, 2011.

[41] D. Korpi, L. Anttila, V. Syrjälä, and M. Valkama, "Widely linear digital self-interference cancellation in direct-conversion full-duplex transceiver," *IEEE J. Sel. Areas Commun.*, vol. 32, no. 9, pp. 1674–1687, 2014.

[42] K. Komatsu, Y. Miyaji, and H. Uehara, "Frequency-domain hammerstein self-interference canceller for in-band full-duplex OFDM systems," in *IEEE Wireless Commun. Netw. Conf. (WCNC)*, 2017, pp. 1–6.

[43] D. Korpi, L. Anttila, and M. Valkama, "Reference receiver based digital self-interference cancellation in MIMO full-duplex transceivers," in *IEEE Globecom Workshops (GC Wkshps)*, 2014, pp. 1001–1007.

[44] H. Krishnaswamy and L. Zhang, "Analog and RF interference mitigation for integrated MIMO receiver arrays," *Proc. IEEE*, vol. 104, no. 3, pp. 561–575, 2016.

[45] X. Huang and J. Guo, "In-band full-duplex technology for future generations of wireless communications," UTS Global Big Data Technol. Centre, White Paper, 2021.

[46] T. Chen, M. B. Dastjerdi, H. Krishnaswamy, and G. Zussman, "Wideband full-duplex phased array with joint transmit and receive beamforming: Optimization and rate gains," in *Proc. ACM Int. Symp. Mobile Ad Hoc Netw. Comput. (MobiHoc)*, 2019, pp. 361–370.

[47] J. P. Doane, K. E. Kolodziej, and B. T. Perry, "Simultaneous transmit and receive performance of an 8-channel digital phased array," in *IEEE Int. Symp. Antennas Propag. USNC/URSI Nat. Radio Sci. Meeting*, 2017, pp. 1043–1044.

[48] E. Everett, C. Shepard, L. Zhong, and A. Sabharwal, "SoftNull: Many-antenna full-duplex wireless via digital beamforming," *IEEE Trans. Wireless Commun.*, vol. 15, no. 12, pp. 8077–8092, 2016.

[49] K. E. Kolodziej, B. T. Perry, and J. S. Herd, "Simultaneous transmit and receive (STAR) system architecture using multiple analog cancellation layers," in *IEEE MTT-S Int. Microw. Symp.*, 2015, pp. 1–4.

[50] N. Honma, M. Tsunezawa, Y. Yamamoto, and Y. Kashino, "Realizing in-band full-duplex MIMO with feasible RF-chain: Key challenges," in *IEEE Conf. Antenna Meas. Appl. (CAMA)*, 2017, pp. 284–287.

[51] L. Lei, N. Saba, and S. G. Razul, "A multichannel self-interference cancellation prototyping system," in *IEEE 5G World Forum (5GWF)*, 2019, pp. 427–432.

[52] M. B. Dastjerdi, N. Reiskarimian, T. Chen, G. Zussman, and H. Krishnaswamy, "Full duplex circulator-receiver phased array employing self-interference cancellation via beamforming," in *IEEE Radio Freq. Integr. Circuits Symp. (RFIC)*, 2018, pp. 108–111.

[53] M. Ayebe et al., "Systematic self-interference mitigation in full duplex antenna arrays via transmit beamforming," in *Proc. IEEE Int. Conf. Electromagn. Adv. Appl. (ICEAA)*, 2023, pp. 158–163.

[54] M. Ayebe, R. Maaskant, S. E. Gunnarson, J. Malmström, M. Ivashina, and H. Holter, "Joint Tx-Rx beamforming for optimal gain and self-interference mitigation in in-band full-duplex arrays: Theory, figures of merit, and validation," *IEEE Antennas Wireless Propag. Lett.*, 2025.

[55] M. Ayebe, R. Maaskant, and M. Ivashina, "Self-Interference–Constrained Transmit Beamforming in Interleaved and Displaced In-Band Full-Duplex Arrays: Gain and Isolation Trade–Offs," in *Proc. IEEE Int. Symp. Antennas Propag. USNC-URSI Radio Sci. Meeting (AP-S/URSI)*, 2026.

[56] M. Ayebe, R. Maaskant, B. Göransson, and H. Holter, "Transmit and receive beamforming for in-band full-duplex mu-mimo under self-interference constraints with measurement-based validation," *IEEE Open J. Antennas Propag.*, 2026.

[57] M. Ayebe, R. Maaskant, J. Malmström, S. E. Gunnarson, H. Holter, and M. Ivashina, "3D-printed silver-coated vivaldi array with integrated coaxial probe feeding," in *Proc. IEEE Int. Symp. Antennas Propag. INC/USNC-URSI Radio Sci. Meeting (AP-S/INC-USNC-URSI)*, 2024, pp. 7–8.

[58] M. Ayebe et al., "In-band full-duplex antenna beamforming and synchronization for self-interference mitigation: Multi-tile RFSoC testbed design and deployment," in *19th Eur. Conf. Antennas Propag. (EuCAP)*, 2025.

[59] M. Ayebe, R. Maaskant, M. Ivashina, H. Holter, and A. Wikström, "Antenna-level self-interference suppression in full-duplex radar via transmit beamforming," *IEEE Antennas Wireless Propag. Lett.*, 2026.

[60] M. Ayebe, R. Maaskant, M. Ivashina, H. Holter, and J. Malmström, "Generative deep-learning design of single-and dual-polarized four-port mimo antennas for full-duplex communication," *IEEE Antennas Wireless Propag. Lett.*, 2026.

[61] K. Kurokawa, "Power waves and the scattering matrix," *IEEE Trans. Microw. Theory Techn.*, vol. 13, no. 2, pp. 194–202, 1965.

[62] K. F. Warnick, D. B. Davidson, and D. Buck, "Embedded element pattern loading condition transformations for phased array modeling," *IEEE Trans. Antennas Propag.*, vol. 69, no. 3, pp. 1769–1774, 2020.

[63] A. Ludwig, "The definition of cross polarization," *IEEE Trans. Antennas Propag.*, vol. 21, no. 1, pp. 116–119, 1973.

[64] H. L. Van Trees, *Optimum Array Processing: Part IV of Detection, Estimation, and Modulation Theory*. John Wiley & Sons, 2002.

[65] R. Maaskant, "Analysis of large antenna systems," Ph.D. dissertation, Eindhoven Univ. Technol., 2010.

[66] C. A. Balanis, *Antenna Theory: Analysis and Design*. John Wiley & Sons, 2016.

[67] N. R. Dusari and M. Rawat, "Practical implementation challenges in MIMO beamforming and its applications," *IEEE Microw. Mag.*, vol. 26, no. 4, pp. 59–75, 2025.

[68] AMD Xilinx, *Zynq ultrascale+ RFSoC RF data converter v2.6 gen 1/2/3/DFE*, `https://docs.amd.com/r/en-US/pg269-rf-data-converter`, 2022.

[69] K. F. Warnick, "Modified element pattern overlap integrals for antenna array mutual impedance estimation," in *Proc. IEEE Int. Symp. Antennas Propag.*, 2025, pp. 1–3.